ELEMENTA
Science of the Anthropocene

Geilfus, N-X, et al. 2023. Gas dynamics within landfast sea ice of an Arctic fjord (NE Greenland) during the spring–summer transition. *Elem Sci Anth*, 11: 1. DOI: https://doi.org/10.1525/elementa.2022.00056

RESEARCH ARTICLE

Gas dynamics within landfast sea ice of an Arctic fjord (NE Greenland) during the spring—summer transition

Nicolas-Xavier Geilfus[1,2,*], Bruno Delille[3], Jean-Louis Tison[4], Marcos Lemes[1], and Søren Rysgaard[1,5,6]

Sea ice is an active component of the Earth's climate system, interacting with both the atmosphere and the ocean. Arctic sea ice is commonly covered by melt ponds during late spring and summer, strongly affecting sea ice physical and optical properties. How melt pond formation affects sea ice gas dynamics and exchanges between sea ice and the atmosphere, with potential feedbacks on climate, is not well known. Here we measured concentrations of N_2, O_2, and Ar, total alkalinity, and dissolved inorganic carbon within sea ice of Young Sound, NE Greenland, to examine how melt pond formation and meltwater drainage through the ice affect its physical properties and gas composition, including impacts on CO_2 exchange with the atmosphere. Sea ice gas composition was controlled mainly by physical processes, with most of the gas initially in gaseous form in the upper ice layer. A minor contribution from biological processes was associated with positive estimates of net community production (up to 2.6 μmol L_{ice}^{-1} d^{-1}), indicating that the ice was net autotrophic. As the sea ice warmed, the upper ice gas concentrations decreased, suggesting a release of gas bubbles to the atmosphere. However, as melt ponds formed, the ice surface became strongly depleted in gases. Due to melt pond development, meltwater permeated through the ice, resulting in the formation of an underwater ice layer also depleted in gases. Sea ice, including brine, slush, and melt ponds, was undersaturated in CO_2 compared to the atmosphere, supporting an uptake of up to −4.26 mmol m^{-2} d^{-1} of atmospheric CO_2. As melt pond formation progressed, however, this uptake weakened in the strongly altered remaining ice surface (the "white ice"), averaging −0.04 mmol m^{-2} d^{-1}. This study reveals the importance of melt pond formation and dynamics for sea ice gas composition.

Keywords: Sea ice, CO_2, Gas, Melt ponds, Carbonate system

1. Introduction

The Arctic Ocean is an important sink for atmospheric carbon dioxide (CO_2), with current estimates of net uptake of CO_2 from −66 to −199 Tg C yr^{-1} (Bates and Mathis, 2009; Takahashi et al., 2009; Yasunaka et al., 2016). The presence of sea ice at high latitudes has been suggested to affect the CO_2 cycle strongly, through the seasonal cycles of sea ice growth and melt (Rysgaard et al., 2011), although the net role of sea ice in terms of air–sea exchanges of CO_2 remains uncertain (Lannuzel et al., 2020). Recent studies have highlighted the complex dynamics of sea ice and its role in CO_2 exchange with the atmosphere, from a strong release of CO_2 towards the atmosphere during initial sea ice growth (9.9 mmol m^{-2} d^{-1}; Geilfus et al., 2013) to a net sink for atmospheric CO_2 as sea ice melts (−9.8 mmol m^{-2} d^{-1}; Van der Linden et al., 2020). While most of the fluxes have been reported in spring and summer (Semiletov et al., 2004; Geilfus et al., 2012; Nomura et al., 2013; Delille et al., 2014; Geilfus et al., 2014; Geilfus et al., 2015), the impacts of melt ponds as contributors to the sea ice CO_2 exchange with the atmosphere and their role in gas dynamics within sea ice remain poorly known, despite the fact that melt ponds are a major and increasing feature of Arctic sea ice (Rösel and Kaleschke, 2012).

Melt ponds have been studied intensively due to their strong impact on the summer energy and mass budgets over sea ice through the sea ice–albedo feedback mechanism (Perovich, 1996; Fetterer and Untersteiner, 1998;

[1] Centre for Earth Observation Science and Department of Environment and Geography, University of Manitoba, Winnipeg, MB, Canada
[2] Current address: Tvärminne Zoological Station, University of Helsinki, Hanko, Finland
[3] Chemical Oceanography Unit, University of Liège, Liège, Belgium
[4] Laboratoire de Glaciologie, DGES-IGEOS, Université Libre de Bruxelles, Bruxelles, Belgium
[5] Greenland Climate Research Centre, Greenland Institute of Natural Resources, Nuuk, Greenland
[6] Arctic Research Centre, Aarhus University, Aarhus, Denmark
* Corresponding author:
Email: nicolas-xavier.geilfus@helsinki.fi

Taylor and Feltham, 2004; Perovich et al., 2011; Polashenshi et al., 2012). Melt ponds result from the accumulation of meltwater (initially from snow, then sea ice) on the surface of relatively impermeable ice. The volume of meltwater is determined by the balance of inflow and outflow, accumulated in the lowest point of local topography. Inflow is based on melting rate, possible precipitation, and the size of the catchment basin of the pond. Outflow depends on the hydraulic pressure gradient in the brine system (Darcy's law) and the presence of outflow pathways such as cracks, leads, or other openings, including seal breathing holes (Polashenski et al., 2012). As sea ice warms, its brine volume increases and meltwater ponds, located above the freeboard, may drain through the ice (i.e., brine flushing; Fetterer and Untersteiner, 1998) to the underlying seawater, freshening the upper layer of the water column. This process can lead to the formation of under-ice melt ponds, where freshwater lenses are trapped under thinner ice areas or in depressions at the bottom of thicker ice (Weeks, 2010). Therefore, melt pond formation not only impacts the physical and optical properties of sea ice (Perovich, 1996; Perovich et al., 2002), but also influences the temporal evolution of sea ice salinity, the carbon and nutrient distributions within the ice matrix, and the salt and heat budget of the ocean mixed layer below (Eicken et al., 2002; Perovich et al., 2002).

Several studies have reported sea ice uptake of atmospheric CO_2 during active surface melt (Semiletov et al., 2004; Geilfus et al., 2012; Nomura et al., 2013; Geilfus et al., 2015). Increasing sea ice temperature, subsequent brine freshening, and dissolution of ikaite (metastable calcium carbonate precipitate, $CaCO_3 \bullet 6H_2O$; Dieckmann et al., 2008) result in a strong decrease of total alkalinity (TA), dissolved inorganic carbon (DIC), and brine partial pressure of CO_2 (pCO_2), causing sea ice to act as a sink for atmospheric CO_2 (Semiletov et al., 2004; Geilfus et al., 2012; Nomura et al., 2013; Delille et al., 2014; Geilfus et al., 2014; Geilfus et al., 2015). This drawdown of pCO_2 is also enhanced by the development of an autotrophic (photosynthesizing) community at the bottom of the sea ice, where more CO_2 is fixed into organic matter than released via respiration (Van der Linden et al., 2020).

However, during sea ice melt, gas inclusions can be created within the ice structure, as water vapor can form inside the brine pockets above the freeboard line or as drained brine pockets and channels are being replaced by atmospheric gases (Tsurikov, 1979). Changes in sea ice physical properties and processes of air inclusion within sea ice can potentially affect the sea ice exchange of gases with the atmosphere. Oxygen (O_2), nitrogen (N_2), and argon (Ar) mainly reside within sea ice in the gaseous form (i.e., bubbles) rather than dissolved within the brine (Zhou et al., 2013; Crabeck et al., 2014; Moreau et al., 2014; Crabeck et al., 2019). The formation of gas bubbles from entrapped brine has been suggested mainly due to the decreasing gas solubility as sea ice temperature and salinity change during sea ice growth (Zhou et al., 2013; Crabeck et al., 2014). Alternatively, gas diffusion has been suggested as a key process controlling gas fluxes across sea ice, even at low brine volume fraction (Gosink et al., 1976; Loose et al., 2009).

Gases can also be produced and/or consumed by organisms living in or under the ice and can be taken up or released during the natural cycle of sea ice formation and melt. The cycles of gases are therefore closely linked to biological processes. Ice algae, phytoplankton and bacterial communities will adapt to changes in sea ice (Lannuzel et al., 2020) with direct consequences for the uptake and release of climate-active gases. Heterotrophic activity and algal production affect the O_2 and CO_2 dynamics within sea ice by releasing or consuming O_2 and CO_2 as well as impacting the concentrations of DIC and TA, both key parameters driving the exchange of CO_2 across the ocean-sea ice-atmosphere interface. During oxic conditions (calcification apart), the contribution of microbial processes to DIC changes is best described by the net community production (NCP). NCP is defined as the difference between gross primary production and ecosystem respiration. The succession of distinct heterotrophic and autotrophic phases has recently been reported in both Arctic and Antarctic sea ice, based on the traditional methods of melted ice core incubations (Søgaard et al., 2010; Campbell et al., 2017) or using the ratio O_2:Ar (Zhou et al., 2014; Van der Linden et al., 2020). Depending on the autotrophic or heterotrophic state of the sea ice, one could expect opposite effects on CO_2 uptake or release between the atmosphere and the sea ice cover.

A common way to estimate the relative contribution of meteoric water (including snow melt) in the marine environment (including sea ice) is to use the stable isotope composition of oxygen in water, $\delta^{18}O$-H_2O (herein referred to as $\delta^{18}O$; Souchez et al., 1988; Macdonald et al., 1995; Eicken, 1998). The $\delta^{18}O$ is expressed in ‰, relative to the Vienna Mean Standard Ocean Water (VSMOW) as:

$$\delta^{18}O\,(‰) = \left[\frac{(R_{sample} - R_{VSMOW})}{R_{VSMOW}}\right] \times 1000 \qquad (1)$$

where $R = {}^{18}O/{}^{16}O$. Both equilibrium thermodynamic and kinetic effects favor the accumulation of lighter isotopes of water in the vapor phase and heavier isotopes in the liquid phase (Craig and Gordon, 1965). Repeated cycles of evaporation and precipitation, as water molecules travel towards the poles, cause polar latitude meteoric water to be depleted in ^{18}O relative to ^{16}O, resulting in more negative $\delta^{18}O$ values in meteoric water compared to seawater. As such, reported values of $\delta^{18}O$ for both glacial ice and snow cover in polar latitudes have ranged from -20‰ to -30‰, with some values as low as -40‰ (Dansgaard and Tauber, 1969; Johnsen et al., 2001). In contrast, sea ice formation slightly favours heavier isotope incorporation into the solid phase (Souchez et al., 1988; Eicken, 1998). Reported $\delta^{18}O$ values typically range from -8‰ to 2‰ (Carnat et al., 2013; Alkire et al., 2015), with values as low as -22‰ (Geilfus et al., 2021), based on the isotopic signature of the surface water signature from which sea ice grew (Macdonald et al., 1995; Geilfus et al., 2021). Therefore, glacial ice and snow will have

distinguishable $\delta^{18}O$ values from that of sea ice and of seawater ($\delta^{18}O$ close to 0‰).

This study presents the changes of physical properties occurring within landfast sea ice during the spring–summer transition in Young Sound, Northeast Greenland. We discuss the relative contribution of physical and biological processes associated with melt pond formation and meltwater drainage, and how these contributions affect the gas composition and dynamics within sea ice and the exchange of CO_2 with the atmosphere.

2. Methods

2.1. Study area

This study was based at the Daneborg field station (74°18 N, 20°13 W), a marine research facility located 25 km southeast of the Zackenberg research station, in Northeast Greenland (**Figure 1**). This fjord system is characterized by an outer part, Young Sound, and an inner part, Tyrolerfjord. The fjord is approximately 90 km long from its mouth to the inner part of Tyrolerfjord, 2 to 7 km wide, and covers about 390 km^2 (Rysgaard et al., 2003). The fjord system is usually covered by landfast sea ice for approximately 9 months of the year, extending up to 10–30 km from the fjord mouth before transitioning to pack ice where a wind-driven shelf polynya has been observed, though it varies in occurrence, location, and size (Pederson et al., 2010). During the year of our observations, sea ice started to form in mid-October 2013 (Kirillov et al., 2015). Several northerly storm events maintained a coastal polynya until early March 2014 after which landfast sea ice covered the polynya area and remained stable until breakup (July 15, 2014; Dmitrenko et al., 2015; Kirillov et al., 2015). During our survey, the middle layer of the water column (40–140 m depth) was filled with cool, saline, and oxygen-enriched polynya water (Dmintrenko et al., 2015). During summer, the fjord is under strong influence of the surrounding glaciers (i.e., Greenland Ice Sheet and local glaciers) as summer runoff from the surrounding catchment areas decreases surface seawater salinity from approximately 33 to 5 in the inner part of the Tyrolerfjord (Bendtsen et al., 2014).

2.2. Sampling procedures

Sea ice cores, snow, and seawater samples were collected during the spring–summer transition, from May 24 to June 24, 2014 (**Table 1**). The sampling site was located across from the research station, a few km within the fjord (74.322°N, 20.269°W; **Figure 1**). At the site, adjacent 5 m × 5 m plots were chosen for snow, sea ice and under-ice seawater sampling. The sea ice in this defined area was assumed to be homogeneous, with six sampling events over time designated as S1–S6. First, snow cover and slush layer (i.e., a mixture of snow and water), when present, were collected using Ziplock bags, with samples stored in a cooler until transported back to the station. Four sea ice cores were collected using a MARK II coring system (internal diameter of 9 cm, Kovacs Enterprises®, Roseburg, OR, USA) for: i) in situ temperature; ii) bulk ice salinity, total alkalinity (TA), dissolved inorganic carbon (DIC), and water stable isotopes ($\delta^{18}O$); iii) chlorophyll-*a* (Chl-*a*) and nutrient (NH_4^+, NO_2^-, NO_3^-, and PO_4^{3-}) concentrations; and iv) argon (Ar), oxygen (O_2) and nitrogen (N_2) gas concentrations. Sea ice cores were wrapped in polyethylene bags immediately after extraction and stored horizontally, to minimize brine drainage, in a cooler containing −20°C eutectic bags. Snow and sea ice in situ temperature was measured using a calibrated temperature probe (Testo 720®, Lenzkirch, Germany, ±0.1°C precision). For sea ice, temperature was measured directly after the core extraction by inserting the temperature probe into pre-drilled holes at 5 to 10 cm vertical resolution.

Surface seawater was collected through a core hole using a peristaltic pump (Cole Palmer®, Masterflex Environmental Sampler) with Tygon® tubing from which the length corresponds to the observed sea ice thickness (plus a few centimeters). Water column samples were also

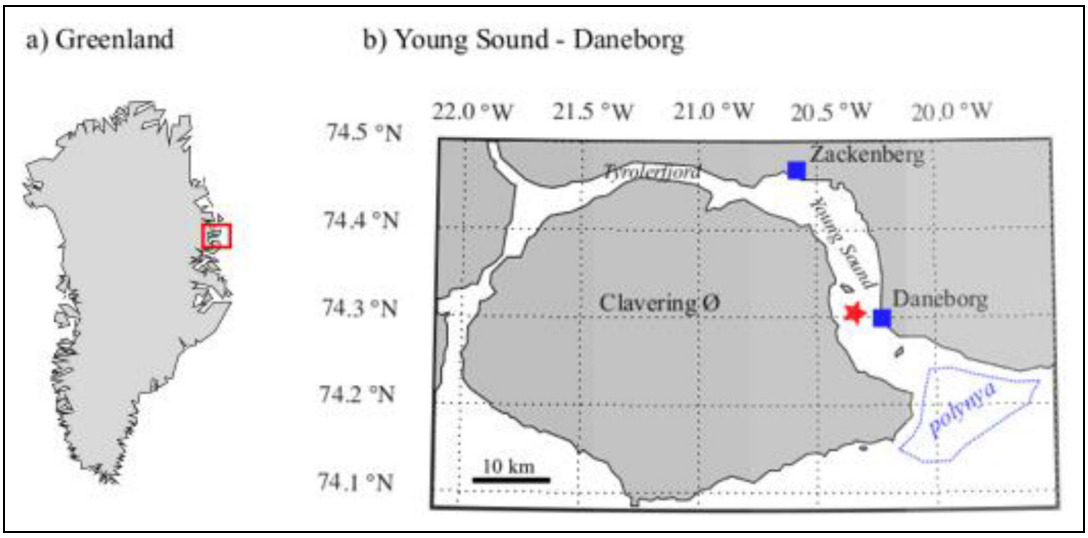

Figure 1. Sampling site location. Location of a) the fjord system (red square) in NE Greenland and b) the sampling site (red star) in Young Sound, including the positions of the Daneborg and Zackenberg research stations and the polynya (dotted blue line).

Table 1. Sampling event, date, and associated sea ice, snow and slush thickness, freeboard, presence of melt ponds, and estimated snow ice thickness

Sampling Event	Sampling Date (2014)	Sea Ice Thickness (cm)	Snow Depth (cm)	Slush Depth (cm)	Freeboard (cm)	Melt Ponds	Snow Ice Thickness (cm)
S1	May 26	137.5	60	Na[a]	5	No	45
S2	May 30	145	50	5	Na	No	55
S3	June 5	143	46	8	−8	No	55
S4	June 11	135	35	3	−3	No	55
S5	June 17	135	20	4	−4	Yes	45
S6	June 23	135	14	8	−8	Yes	35

[a] Not measured or not applicable.

collected at 1, 2.5, 10, 20, 30, 50, and 100 m using 5 L Niskin bottles. Seawater samples were collected using sealed glass 100 mL BOD bottles. A headspace of 1% of the bottle volume was introduced to accommodate thermal expansion. Vertical profiles of water temperature and salinity were measured with a newly factory-calibrated Sea-Bird SBE 19plus V2 (Sea-Bird Scientific, Bellevue, WA, USA) conductivity-temperature-depth (CTD) probe, accurate to ±0.005°C and ±0.0005 S m^{-1} (Dmitrenko et al., 2015).

A few meters away from the sampling site, a soil CO_2 flux system was deployed with four long-term deployment automatic chambers (LI-COR® 8100-104, Lincoln, NE, USA). Chambers for CO_2 flux measurements were deployed on snow-covered sea ice surfaces. Each chamber closed and measured fluxes for 15 min every hour, while remaining open the rest of the time to avoid surface disturbance as much as possible. Chamber maintenance was performed every day, while chamber repositioning to unaltered surface was performed when snow drift was accumulating and preventing chamber closure or when sea ice was too altered by melting to ensure proper sealing of the collar between the ice and the chamber. The chambers consist of an automated moveable metal dome (internal diameter = 20 cm, height = 9.7 cm), closed at the top by a pressure vent designed to maintain an ambient pressure inside under calm and windy conditions. A rubber seal surrounds the soil collar and ensures an airtight connection at the chamber-ice interface. The metallic soil collar has been designed for sea ice measurements with serrated circumference to allow its penetration into the ice. For measurements over snow, a stainless-steel tube was mounted at the base of the chamber and pushed down to the ice to enclose snow and prevent lateral diffusion of air in the snowpack.

The chambers were temporarily closed above the snow or ice interface and connected using a multiplexer (LI-COR® LI-8150, Lincoln, NE, USA) to an infrared gas analyzer (LI-COR® LI-8100A, Lincoln, NE, USA) recording the air pCO_2 during a designated time interval (30 min). The flux was determined by measuring the change of air pCO_2 within the chamber. Flux calculations were performed routinely using the LI-COR® SoilFluxPro software, with volumes adjusted to include collar offsets (i.e., rim height above the surface) and applying water vapor corrections for dilution and band broadening. The fluxes were determined by the slope of the linear or exponential regression of pCO_2 over time, depending on the best fit. All fluxes were visually checked to discard measurements biased by contamination or poor sealing of the chamber. The detection limit was ±0.004 μmol m^{-2} s^{-1}. Fluxes below the detection limit were considered as null. The uncertainty of the flux computation due to the standard error of the regression slope was ±8%.

2.3. Sample analysis

Back at the station, seawater samples were transferred to gas-tight vials (12 mL Exetainer, Labco High Wycombe, UK), poisoned with 12 μL solution of saturated $HgCl_2$, and stored in the dark at room temperature until analysis for TA and DIC. Water aliquots of 2 mL were also collected in fully filled gas-tight glass vials for $\delta^{18}O$ measurements, with salinity measured on the remaining sample volume. A sea ice core dedicated to bulk ice salinity and the carbonate system was cut into 5–10 cm sections. Each section was immediately placed into a gas-tight laminated (Nylon, ethylene vinyl alcohol and polyethylene) plastic bag (Hansen et al., 2000) fitted with a 20 cm gas-tight Tygon tube and valve. The plastic bag was sealed, and excess air was gently removed through the valve using a vacuum pump. Snow and slush samples were processed following the same procedure. Bagged sea ice, slush, and snow samples were then melted at room temperature. As soon as samples were completely melted, meltwater was transferred to gas-tight vials (12 mL Exetainer, Labco High Wycombe, UK), poisoned with 12 μL solution of saturated $HgCl_2$, and stored in the dark at room temperature until analysis for TA and DIC. Water aliquots of 2 mL were also collected in fully-filled gas-tight glass vials for $\delta^{18}O$ measurements, with salinity measured on the remaining volume of meltwater.

For Chl-*a* and nutrient (NO_3^-, NO_2^-, PO_4^{3-}, and NH_4^+) analyses, the dedicated ice core was cut into 10 cm sections and melted in the dark, at room temperature. Snow and slush samples were melted following the same procedure, without adding pre-filtered seawater, as suggested

by Rintala et al. (2014). Soon after complete melting, samples for Chl-*a* determination were filtered using Whatman GF/C glass-fibre filters (which may underestimate Chl-*a* content compared to GF/F filters of smaller effective pore size). Filters were stored frozen in aluminium foil until measurement at the home laboratory; 50 mL of the filtrate was kept frozen for nutrient analyses. Filters were extracted in 10 mL acetone at 4°C for 16 h. Chl-*a* concentrations were determined using a Turner Design TD700 fluorometer. Nitrate plus nitrite ($[NO_3^-]$ + $[NO_2^-]$, later noted as NO_x^-) was measured using the sulfanilamide colorimetric method; ammonium ($[NH_4^+]$), with the dichloroisocyanuratesalicylate-nitroprussiate colorimetric method, and phosphate ($[PO_4^-]$), with the ammonium molybdate-potassium antimonyl tartrate method (Westwood, 1981; American Public Health Association, 1998). Analyses were made colorimetrically using a 5-cm optical path, with a Genesys 10 vis spectrophotometer (Thermo Fisher Scientific, Waltham, Massachusetts, USA). The detection limits of the methods were 0.15, 0.03, 0.3, and 0.06 µmol L^{-1} for NO_3^-, NO_2^-, NH_4^+, and PO_4^- respectively.

Salinity was calculated based on conductivity (Grasshoff, 1983) measured using a meter (Orion 3-star, Thermo Scientific, Walham, MA, USA) coupled with a conductivity cell (Orion 013610MD, Thermo Scientific) with a precision of ±0.1. Brine volume was estimated from measurements of bulk ice salinity, temperature, and density according to Cox and Weeks (1983) for temperatures below −2°C and according to Leppäranta and Manninen (1988) for ice temperatures between −2°C and 0°C. $\delta^{18}O$ was measured on an isotope analyzer (Picarro L2130-*i*, Santa Clara, CA, USA) with a precision of 0.025‰, calculated as the standard deviation from 9 repeated measurements of standard materials.

TA was determined by Gran titration (Gran, 1952) using a TIM 840 titration system (Radiometer Analytical, ATS Scientific, Burlington Ontario, Canada), consisting of a Ross sure-flow combination pH glass electrode (Orion 8172BNWP, Thermo Scientific) and a temperature probe (Radiometer Analytical, Lyon, France). A 12 mL sample was titrated with a standard 0.05 M HCl solution (Alfa Aesar, Haverhill, MA, USA). DIC was measured on a DIC analyzer (Apollo SciTech, Newark, DE, USA) by acidification of a 0.75 mL subsample with 1 mL 10% H_3PO_4 (Sigma-Aldrich, Saint-Louis, MO, USA), and quantification of the released CO_2 with a nondispersive infrared CO_2 analyzer (LI-COR, LI-7000, Lincoln, NE, USA). Results were then converted from µmol L^{-1} to µmol kg^{-1} based on sample density, which was estimated from salinity and temperature at the time of the analysis. Accuracies of ±3 and ±2 µmol kg^{-1} were determined for TA and DIC, respectively, from routine analysis of certified reference materials (A.G. Dickson, Scripps Institution of Oceanography, San Diego, CA, USA). From TA and DIC measurements, pCO_2 is calculated by the CO2sys program (Pierrot et al., 2006) using the dissociation constants from Mehrbach et al. (1973) refitted by Dickson and Millero (1987), assuming these constants are valid for the range of temperatures and salinities encountered within sea ice (Papadimitriou et al., 2004). Those constants were selected as they have shown good agreement between measured and calculated values in Arctic waters (Chen et al., 2015; Wooseley et al., 2017).

Analysis for O_2, N_2, and Ar concentrations in sea ice (denoted $[O_2]$, $[N_2]$, and [Ar]) were performed by gas chromatography. The gas phase was extracted from the ice using the dry-crushing technique, initially developed for gas measurements in continental ice (Raynaud et al., 1982). The sea ice core was cut into 5 cm sections, and 60 g of each section was placed into a vessel together with stainless steel beads. The sample was then crushed in the vessel at a temperature of −25°C and under a vacuum of 10^{-3} Torr, allowing the extraction of both gas bubbles and dissolved gas within sea ice brines (Stefels et al., 2012). The vessel, kept at −25°C in a cold ethanol bath, was then connected to the gas chromatograph equipped with a thermal conductivity detector for concentration analyses. AlphagazTM2 He (Air liquid®—P0252) was used as the carrier gas and a 22 mL packed column (Mole Sieve 5A 80/100; 5 m × 1/8″). Precision of analysis was 0.7% for O_2 and N_2, and 2.2% for Ar (Zhou et al., 2014).

The amount of gas collected (i.e., $[O_2]$, $[N_2]$, and [Ar], in µmol L_{ice}^{-1}) includes both the gas bubbles from the ice and the dissolved phase within sea ice brine. Therefore, measured gas concentrations are compared to their respective maximum concentrations in bulk ice when sea ice brines are at atmospheric saturation (denoted $[O_2]_{sat}$, $[N_2]_{sat}$, and $[Ar]_{sat}$). The latter represents the maximum concentration of O_2, N_2, or Ar in the dissolved phase, if no supersaturation exists in the brine (Zhou et al., 2013; Crabeck et al., 2014), and is calculated based on respective temperature and salinity-dependent solubility coefficients (Garcia and Gorden, 1992; Hamme and Emerson, 2004), using brine temperature and salinity, brine volume fraction, and sea ice density to express the value in micromoles per liter of bulk ice (Crabeck et al., 2014). These estimates have been suggested to remain valid for the range of temperature and salinity observed in sea ice (Zhou et al., 2013).

According to Crabeck et al. (2014), the difference between observed gas concentration measured in bulk ice (i.e., $[O_2]$, $[N_2]$, and [Ar], denoted [X]) and their respective maximum concentrations when brines are at saturation (i.e., $[O_2]_{sat}$, $[N_2]_{sat}$, and $[Ar]_{sat}$) provides an estimate of gas concentration in the ice that resides in the gas phase (i.e., the gas content of bubbles, denoted $[O_2]_{bub}$, $[N_2]_{bub}$, and $[Ar]_{bub}$), assuming no supersaturation within sea ice brines and that the sum of gas partial pressure is above 1 atm. If the latter condition is correct from a thermodynamical standpoint, then bubble formation could not be entirely related to the thermodynamical conditions, as interfacial bubble nucleation processes and supersaturation of gases in the liquid phase have been reported previously (Jones et al.,1999; Tison et al., 2016) and pressures higher than atmospheric have also been suggested to exist within sea ice brines (Crabeck et al., 2019). Therefore,

$$[X]_{bub} = [X] - [X]_{sat} \quad (2)$$

with the percent gas content in the bubbles (f_{bub}) estimated as

$$f_{bub} = \left({}^{[X]_{bub}} \Big/ _{[X]} \right) \times 100 \quad (3)$$

and the supersaturation factor (Sat_f, in %) estimated by

$$Sat_f = {}^{[X]} \Big/ _{[X]_{sat}} \times 100 \quad (4)$$

where X corresponds to either O_2, N_2, or Ar.

To estimate the net community production (NCP) from the $[O_2]$:[Ar] ratio, we used the method developed by Zhou et al. (2014) and Tison et al. (2017), modified by Van der Linden et al. (2020). We first calculated the $[O_2]$:[Ar] deviation from saturation as:

$$\Delta(O_2/Ar) = \frac{[O_2]/[Ar]}{[O_2]_{sat}/[Ar]_{sat}} - 1 \quad (5)$$

Equilibrium concentrations of O_2 and Ar can differ from their solubility due to physical processes. To account for potential biases using O_2 and Ar solubilities for $[O_2]$ and [Ar], we estimated the impact of physical processes on O_2 concentration (i.e., bubble formation and migration, brine movements, $[O_2]_{phys}$), using [Ar] as a witness of physical processes only:

$$[O_2]_{phys} = [O_2]_{sat} \times \left([Ar]/[Ar]_{sat} \right) \quad (6)$$

From there, the O_2 concentration associated with in situ biological activity is obtained by:

$$[O_2]_{bio} = [O_2]_{phys} \times \Delta(O_2/Ar) \quad (7)$$

$[O_2]_{bio}$ is expressed in µmol L_{ice}^{-1}.

NCP is then determined from the change of oxygen concentration associated with in situ biological activity ($[O_2]_{bio}$) as:

$$NCP = \frac{[O_2]_{bio}(t_{s+1}) - [O_2]_{bio}(t_s)}{\Delta t} \quad (8)$$

where Δt represents the elapsed time between two sampling events (see **Table 1**), and t_s and t_{s+1} correspond to the sampling event s and the next sampling event (s+1), respectively.

Thin sections are used to show ice crystal texture and bubble content. Thin section analysis provides information regarding the conditions during sea ice formation (Eicken, 2003). Within a cold room set at −25°C, vertical ice core sections were first thinned to about 1.5 cm thickness and stuck onto a glass plate by freezing a small amount of distilled water along its perimeter. Ice sections were then thinned to a few millimeters using a microtome (Leica SM2400, Concord, Ontario, Canada). Thin sections were detached from the glass plate by controlled warming from below, turned over and reattached through melting and refreezing of the thin melted ice interface, a procedure that has been shown not to alter the original ice crystallographic properties (Omstedt, 1985). Thin sections were then thinned further to about 600–700 µm using the microtome and examined on a light table equipped with cross-polarized sheets. The textural types were identified visually based on the size, shape, and orientation of the ice crystals and compared to descriptions found in the literature (e.g., Eicken and Lange, 1991; Eicken, 2003).

3. Results

3.1. Snow cover

Over the survey, the snow thickness decreased from 60 cm (S1) to 14 cm (S6; **Table 1** and **Figure 2**). During the first sampling events, a strong temperature gradient was observed within the snow cover, with temperature increasing from −4.5°C at the snow-ice interface to −0.7°C at the interface with the atmosphere. As the atmospheric temperature increased (presented later), the snow cover thinned, and the temperature gradient progressively disappeared (**Figure 2a**). Maximum salinity, observed at the snow-ice interface, decreased from 14.5 (S2) to 0.4 (S6; **Figure 2b**). The presence of a slush layer (dotted line in **Figure 2**) was first observed at S2 with a salinity of 30.6 and temperature of −1.9°C. As the snow cover melted, slush salinity decreased to a salinity of 0.1 at S6. Melt ponds were first sampled at S5 (dashed line in **Figure 2**) and exhibited positive temperature (0.1°C) and low salinity.

Highly depleted $\delta^{18}O$ values (minima = −21.4‰) were observed at the surface layer of the snow cover (**Figure 2c**). Throughout the snowpack, $\delta^{18}O$ increased with maxima (up to −5.2‰) observed at the snow-ice interface. Slush $\delta^{18}O$ values decreased from −3.0‰ (S2) to −12.8‰ (S6) while in melt ponds, $\delta^{18}O$ averaged −13.6‰ (SD = 0.2, n = 2).

Low TA and DIC, averaging 59 (SD = 11, n = 6) and 45 (SD = 15, n = 6) µmol kg^{-1}, respectively, were observed in the upper 30 cm of the snow cover (**Figure 2d** and **e**). Snow TA and DIC increased towards the snow-ice interface, with maxima of 1178 and 1120 µmol kg^{-1}, respectively. Over time, slush TA and DIC decreased from 2141 to 92 µmol kg^{-1} and from 2028 to 107 µmol kg^{-1}, respectively. TA and DIC concentration in melt ponds closely followed the overall trend observed in the slush, with TA and DIC decreasing from 252 to 76 µmol kg^{-1} and from 235 to 82 µmol kg^{-1}, respectively. Both slush and melt ponds were undersaturated in CO_2 compared to the atmosphere (401 µatm). Slush pCO_2 ranged from 49 (S5) to 284 (S2 and S3) µatm, while melt ponds pCO_2 ranged from 19 (S5) to 83 (S6) µatm (**Figure 2j**).

Within the snow cover, Chl-*a* concentrations ranged from 0.0 to 0.22 µg L^{-1}, while within slush Chl-*a* ranged from 0.0 to 0.81 µg L^{-1} (**Figure 2f**). No measurements were made on melt pond samples. Nutrient concentrations <10 µM were observed within snow, slush, and melt ponds. NO_x^- concentration ranged from 0.77 to 9.48 µM within the snow cover (**Figure 2g**) and increased in the slush, from 0.05 at S2 to 5.33 µM at S6. PO_4^- concentration ranged from 0.0 to 0.25 µM (**Figure 2h**) in the snow cover, while slush concentration decreased from 0.55 at S2 to 0 at S6. NH_4^+ concentrations ranged from 0.0 to 5.0 µM (**Figure 2i**) in the snow cover and from 0 to 3.0 in the slush.

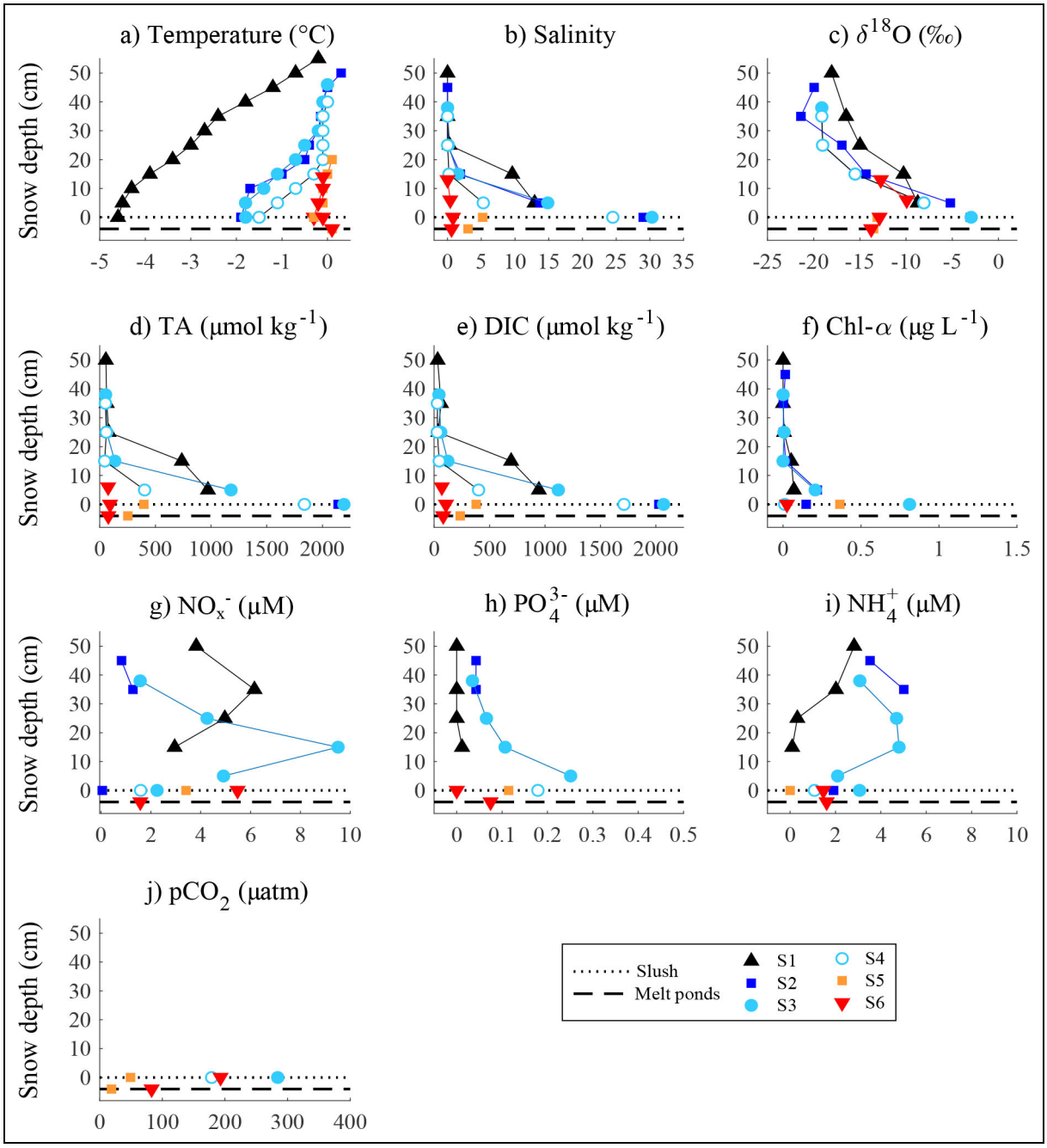

Figure 2. Snow, slush, and melt pond properties. Depth profiles of a) temperature (°C), b) salinity, c) $\delta^{18}O$ (‰), and concentrations of d) total alkalinity (TA; µmol kg^{-1}), e) dissolved inorganic carbon (DIC; µmol kg^{-1}), f) chlorophyll-*a* (Chl-*a*; µg L^{-1}), g) NO_2^- + NO_3^{-1} (NO_x^-; µM), h) PO_4^{3-} (µM), i) NH_4^+ (µM), and j) pCO_2 (µatm). The 0 cm depth corresponds to the snow–ice interface. Slush values are displayed on the black dotted line while melt ponds values are on the black dashed line. S1–S6 refer to progressive sampling events over time (**Table 1**) at the sampling site (**Figure 1**).

3.2. Sea ice

Sea ice thickness remained relatively stable over the survey, ranging from 135 to 145 cm thick (**Table 1** and **Figure 3**). Relatively warm temperatures were observed at the ice interface with both the snow cover and the water column. Sea ice temperature increased consistently (**Figure 3a**) from −1.8°C to −0.1°C in the upper section of the sea ice, and from −1.8°C to −0.2°C in the bottom sea ice section. Overall, bulk ice salinity initially exhibited a typical C-shaped profile (Eicken, 1992), with maximum salinity of 8.2 observed in the upper section of the sea ice (S1; **Figure 3b**). In addition, a local minimum can be observed at 25–30 cm depth in S1 to S5. Over the survey, bulk ice salinity gradually decreased to form an inversed C-shape, with lower salinity observed in the upper and lower sea ice section at S5 and S6. Based on the measured temperature and salinity, the calculated brine volume fraction was consistently above the permeability threshold (i.e., 5% from Golden et al., 2007, or 7% from Zhou et al., 2013), with higher brine volume content in both the

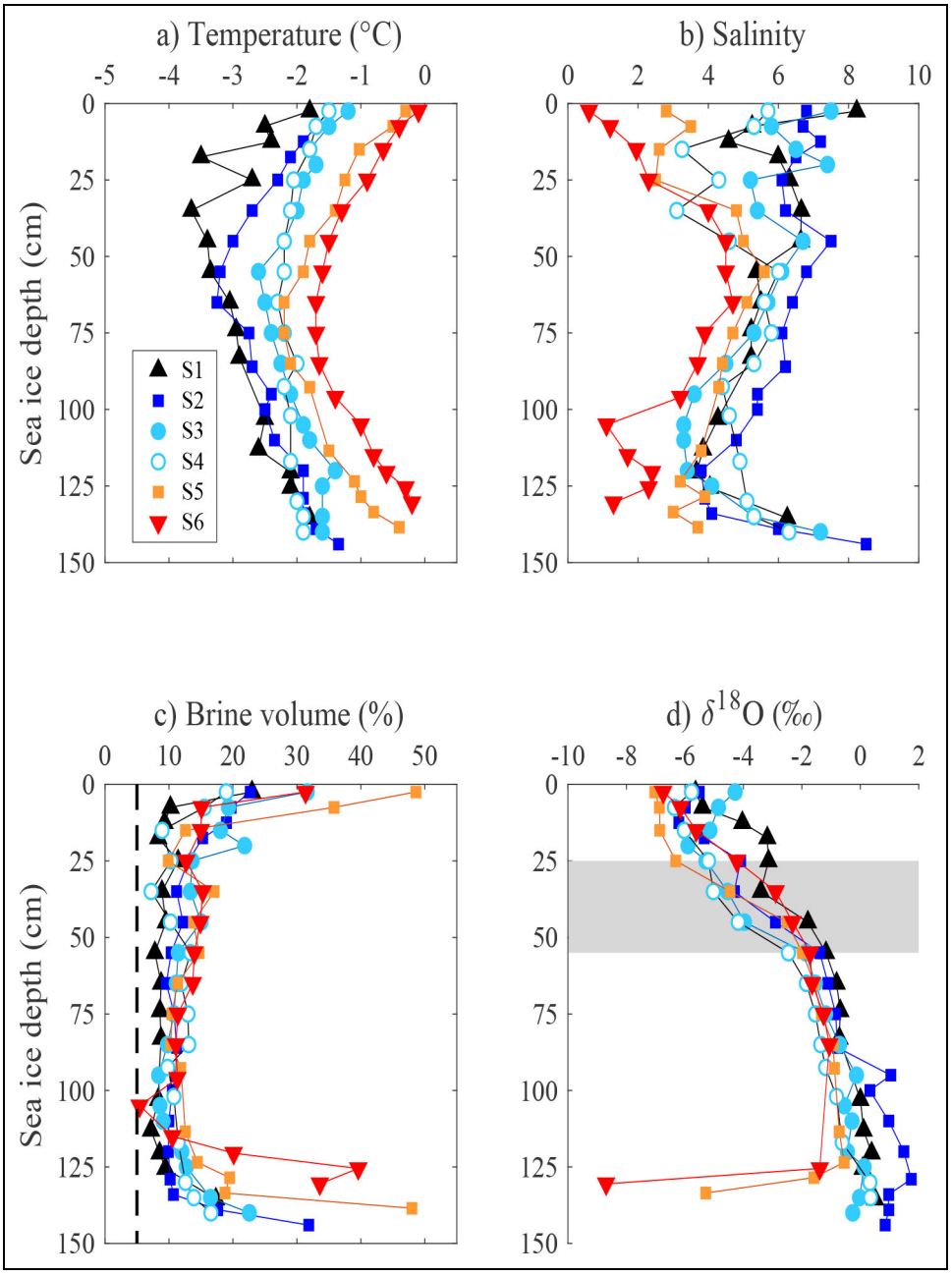

Figure 3. Sea ice physical properties. Depth profiles of a) temperature (°C), b) bulk ice salinity, c) brine volume content (%; the dashed line represents the permeability threshold, i.e., 5% brine volume content; Golden et al., 2007), and d) $\delta^{18}O$ (‰). The grey area in d) represents the transition layer in $\delta^{18}O$ values. S1–S6 refer to progressive sampling events over time (**Table 1**) at the sampling site (**Figure 1**).

upper (up to 51%) and the lower (up to 49%) sections of the sea ice (**Figure 3c**). Sea ice $\delta^{18}O$ values ranged from −9.6‰ to 1.7‰ (**Figure 3d**). The upper 25 cm of the sea ice was strongly depleted in $\delta^{18}O$ (<−5‰), followed by steeply increasing $\delta^{18}O$ values in the 25–55 cm section of the ice column (grey area in **Figure 3d**), after which a moderated increase in $\delta^{18}O$ values was observed throughout the ice thickness in most cases. Unlike the other sampling events, bottom values of $\delta^{18}O$ at S5 and S6 became more depleted at the sea ice interface with the water column, down to −5.3‰ and −8.7‰, respectively.

Concentrations of Chl-*a* and nutrients observed within the sea ice (**Figure 4**) were in the range of concentrations reported previously in the area for the same time period (Rysgaard and Glud, 2004). Chl-*a* concentrations ranged from 0.0 to 1.39 μg L^{-1} (**Figure 4a**). Highest concentrations were observed at S5, with a local maximum at the sea ice interface with the snow cover (0.9 μg L^{-1}) and an increase towards the bottom of the ice column (1.35 μg L^{-1}). NH_4^+ concentrations averaged 1.13 μM (SD = 0.8, n = 91) with values ranging from 0.02 μM to 2.89 μM (**Figure 4b**). PO_4^{3-} concentrations averaged 0.59 μM (SD = 1.32, n = 92; **Figure 4c**). From S1 to S5, the PO_4^{3-} concentration remained stable, with an average value of 0.18 μM (SD = 0.41, n = 81). At S6, the PO_4^{3-} concentration increased, averaging 2.8 μM (SD = 2.2, n = 15) and roughly

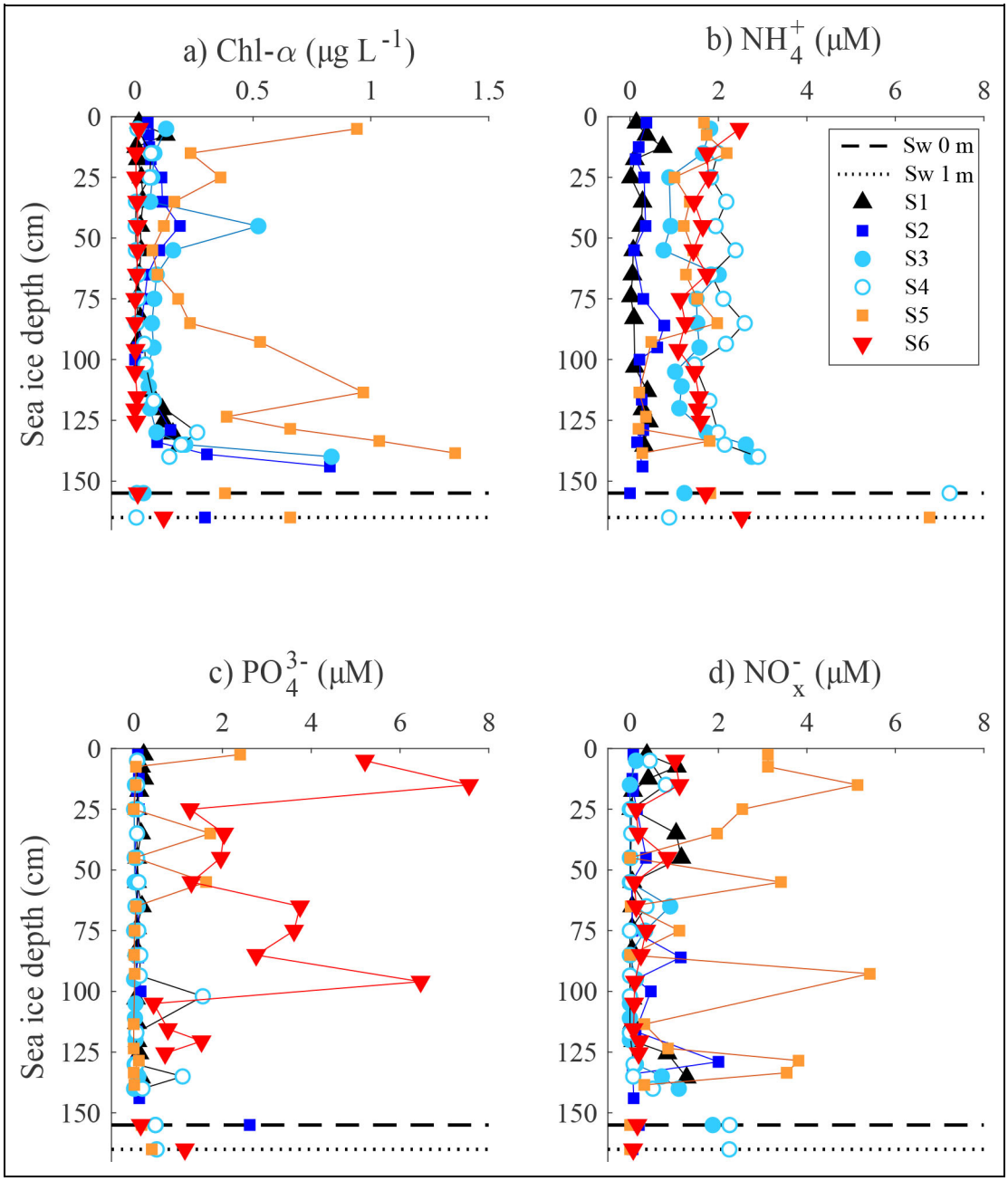

Figure 4. Sea ice and surface seawater biological properties. Depth profiles of concentrations of a) chlorophyll-*a* (Chl-*a*; µg L^{-1}), b) NH_4^+ (µM), c) PO_4^{3-} (µM) and d) $NO_2^- + NO_3^-$ (NO_x^-; µM). Seawater (Sw) concentrations at depths of 0 m and 1 m are presented on dashed and dotted lines, respectively. S1–S6 refer to progressive sampling events over time (**Table 1**) at the sampling site (**Figure 1**).

mimicking S5 profiles of Chl-*a*, with a maximum value of 7.55 µM in the upper sea ice section. NO_x^- concentrations ranged from 0.0 µM to 6.15 µM (**Figure 4c**). S5 exhibited higher concentrations (averaging 2.34 µM, SD = 1.96, n = 17) compared to the other stations (averaging 0.29 µM, SD = 0.38, n = 75).

TA and DIC concentrations measured in bulk melted sea ice ranged from 64 to 657 µmol kg^{-1} and from 52 to 622 µmol kg^{-1}, respectively (**Figure 5a** and **d**). TA and DIC exhibited similar profiles as for bulk ice salinity, with C-shaped profiles from S1 to S4 and inverse C-shaped profiles for S5 and S6, where lower TA and DIC were observed in both upper and bottom sea ice sections. Both TA and DIC correlated strongly with salinity changes (**Figure 5c** and **f**), except for S1, where TA and DIC were higher and lower, respectively, than expected from salinity changes. To discard concentration and dilution effects, sea ice TA and DIC were normalized to the average bulk salinity of 4.5 (denoted as *n*TA and *n*DIC, respectively; **Figure 5b** and **e**): *n*TA averaged 390 µmol kg^{-1} (SD = 103, n = 48) and *n*DIC averaged 350 µmol kg^{-1} (SD = 83, n = 48). Based on sea ice temperature and salinity, we estimated the brine volume content (**Figure 3c**), as well as brine salinity according to the equations from Eicken (2003). Assuming that TA and DIC are contained mainly within the brine, we used the in-situ sea ice temperature, calculated brine

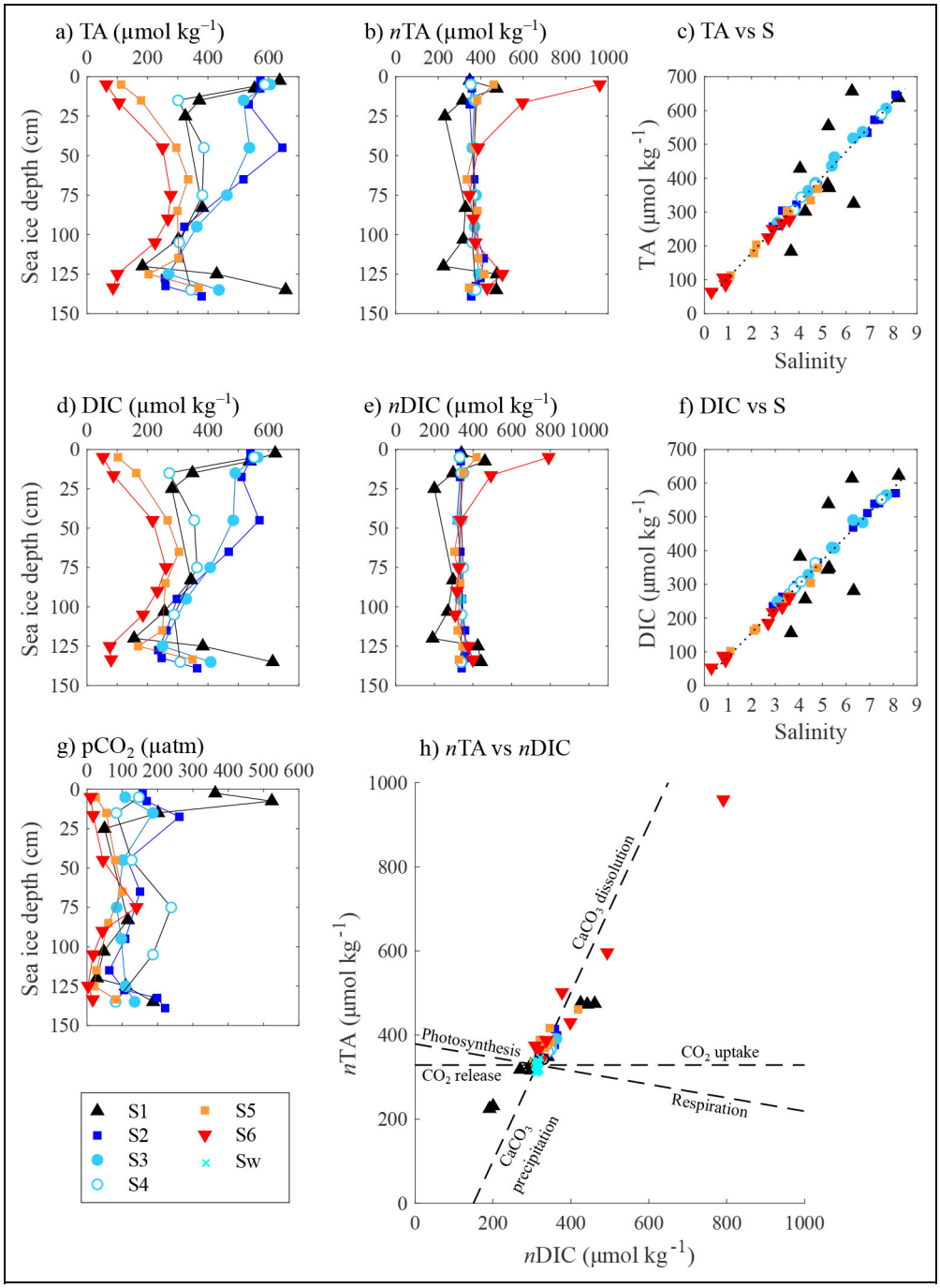

Figure 5. Carbonate system within the sea ice. Depth profiles of a) total alkalinity (TA; µmol kg^{-1}) and b) TA normalized to the average salinity (S) of 4.5 (*n*TA; µmol kg^{-1}), with c) the relationship between TA and S; depth profiles of d) dissolved inorganic carbon (DIC; µmol kg^{-1}) and e) salinity-normalized DIC (*n*DIC, S = 4.5; µmol kg^{-1}), with f) the relationship between DIC and salinity; and depth profiles of g) in-situ brine pCO_2 (µatm), with h) the relationship between *n*TA and *n*DIC. In panel (h), the dashed lines represent the theoretical changes following precipitation/dissolution of calcium carbonate, release/uptake of $CO_{2(g)}$, and biological activity (photosynthesis/respiration). S1–S6 refer to progressive sampling events over time (**Table 1**) at the sampling site (**Figure 1**).

salinity, TA, and DIC to calculate the in-situ brine pCO_2 (as further described in Section 3.3). Brine pCO_2 was undersaturated in CO_2 compared to the atmosphere, with values ranging from 363 (S1) to 3 (S6) µatm, except in the uppermost ice at S1, where a pCO_2 of 523 µatm was estimated (**Figure 5g**). In **Figure 5h**, the ratio between *n*TA and *n*DIC from both sea ice and seawater (also normalized to a salinity of 4.5) is used to investigate the main processes affecting the carbonate system. Dashed lines in **Figure 5h** represent the theoretical response of TA and DIC to different processes. In the case of $CO_{2(g)}$ exchanges, only DIC is affected, while precipitation and dissolution of calcium carbonate ($CaCO_3$) will affect TA and DIC at a ratio of 2:1. Biological activity (photosynthesis/respiration) will affect

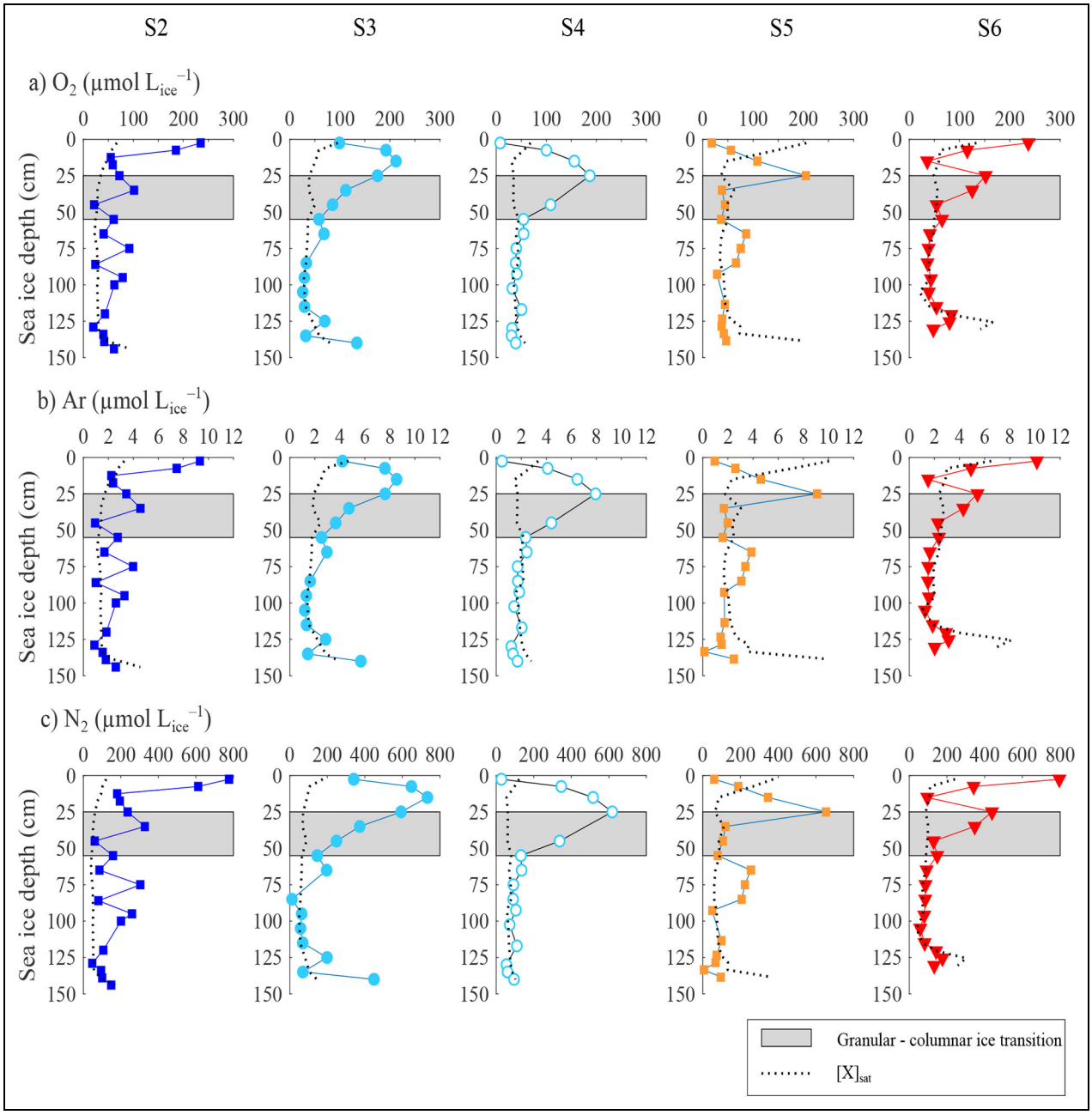

Figure 6. Gas concentrations within the sea ice. Depth profiles of a) O_2 (µmol L_{ice}^{-1}) b) Ar (µmol L_{ice}^{-1}), and c) N_2 (µmol L_{ice}^{-1}). The dotted line represents the maximum gas concentration in sea ice when brines are at saturation. The grey area represents the granular-columnar ice transition, as defined by the $\delta^{18}O$ (**Figure 4**). S1–S6 refer to progressive sampling events over time (**Table 1**) at the sampling site (**Figure 1**).

both TA and DIC at a ratio of −0.16 (Lazar and Loya, 1991). While most of the bulk ice data aligned with the theoretical trend of calcium carbonate dissolution, a few data points from S1 aligned with the theoretical trend of calcium carbonate precipitation.

The evolution of $[O_2]$, [Ar], and $[N_2]$ in bulk sea ice (**Figure 6**) is compared to their respective maximum concentrations in bulk ice when brines are at atmospheric saturation (i.e., $[O_2]_{sat}$, $[N_2]_{sat}$, and $[Ar]_{sat}$; black dotted line in **Figure 6**). Overall, $[O_2]$ ranged from 1 to 237 µmol L_{ice}^{-1} (averaging 73 µmol L_{ice}^{-1}, SD = 54, n = 73), [Ar] ranged from 0 to 10 µmol L_{ice}^{-1} (averaging 3 µmol L_{ice}^{-1}, SD = 2, n = 73), and $[N_2]$ ranged from 5 to 796 µmol L_{ice}^{-1} (averaging 208 µmol L_{ice}^{-1}, SD = 192, n = 73). At S2, gas concentrations were generally higher than $[X]_{sat}$, with the maximum concentration observed at the ice-snow interface. Gas concentrations in the bottom 20 cm were similar to $[X]_{sat}$ or slightly lower. At S3, gas concentration at the ice-snow interface decreased, reaching $[X]_{sat}$. Maximum concentrations were observed at about 20 cm depth. In the upper 75 cm, gas concentrations were higher than their respective $[X]_{sat}$, while below 75 cm they aligned with $[X]_{sat}$ (except for the bottom value). At S4 and S5, gas concentrations are mostly aligned with $[X]_{sat}$, except in the upper 50 cm (S4) and at 25 cm depth (S5) where maximum gas concentrations were observed. For both

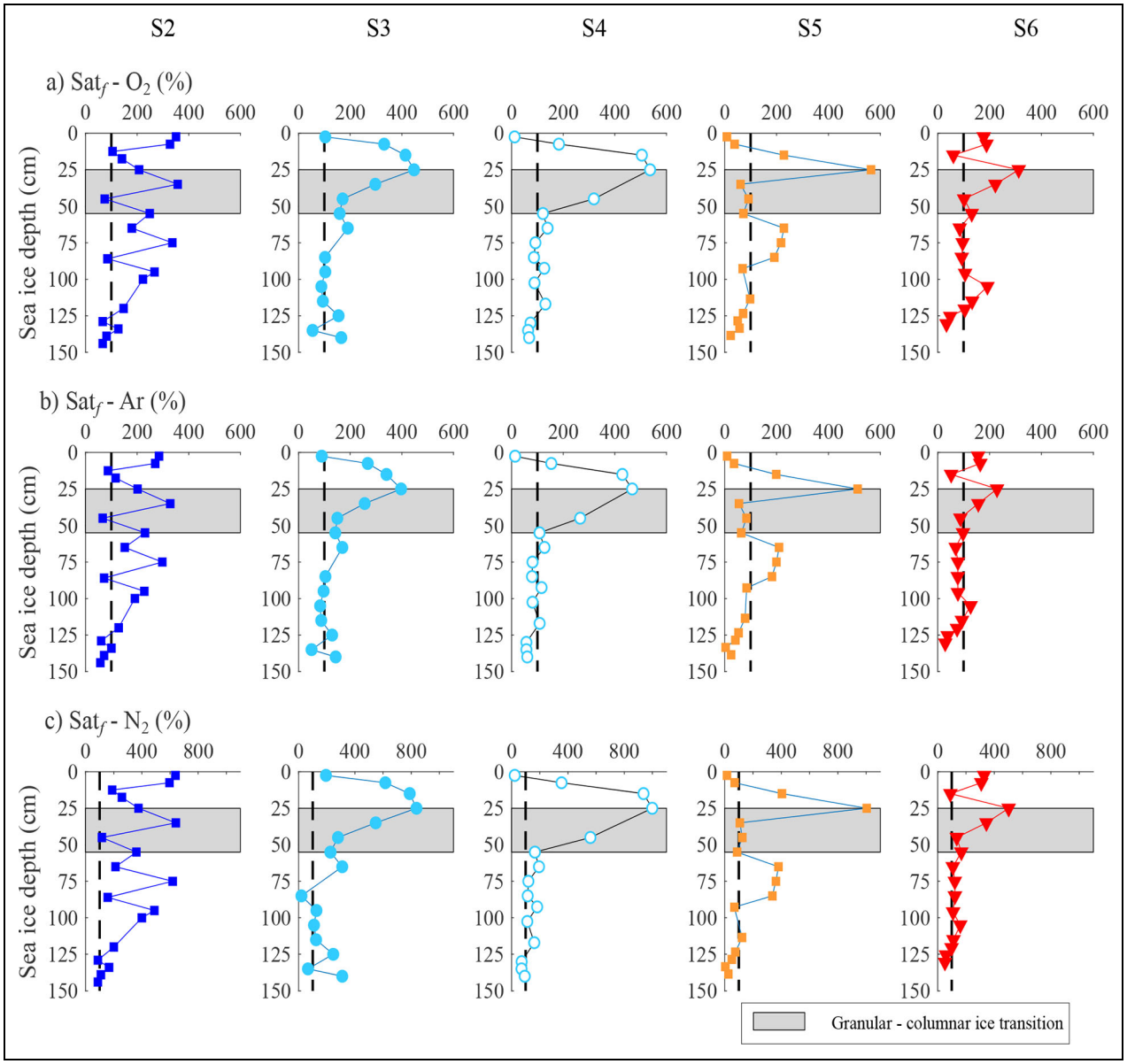

Figure 7. Gas saturation within the sea ice. Depth profiles of a) O_2, b) Ar, and c) N_2 saturation (in %) within the sea ice. The dashed line represents the 100% atmospheric saturation. The grey area represents the granular-columnar ice transition, as defined by the $\delta^{18}O$ (**Figure 4**). S1–S6 refer to progressive sampling events over time (**Table 1**) at the sampling site (**Figure 1**).

S4 and S5, minimum gas concentrations were observed at the sea ice surface (with lowest values at S4). At S6, gas concentrations were slightly higher than $[X]_{sat}$ for most of the ice thickness, with a strong increase at the sea ice surface where maximum concentrations were observed. For all gases, the bottom 5–15 cm at S5 and S6 are strongly undersaturated.

The saturation factor (Sat_f; **Figure 7**) ranged from 9% to 564% for O_2, from 4% to 513% for Ar, and from 5% to 1003% for N_2. The maximum Sat_f was systematically observed at 25 cm below the ice surface, while the minimum was observed in the permeable bottom 15 cm of the sea ice and at the ice-snow interface (S4 and S5). N_2 was the most supersaturated gas species, averaging 259% (SD = 2.38, n = 80), compared to O_2 averaging 162% (SD = 1.22, n = 80) and Ar averaging 139% (SD = 1.06, n = 80). Early in the survey (S2) most of the gas content was in bubbles (**Figure 8**), with maximum bubble content estimated in the upper part of the sea ice. From S3 to S5, the ice-snow interface had minimal bubble content, while most of the bubbles were centred at 25 cm depth. Almost no bubbles were present in the bottom 75 cm sea ice section. At S6, bubble content increased throughout the entire ice thickness.

3.3. Underlying seawater

Seawater temperatures were only recorded during the first half of the survey (S1 to S3) and ranged from −1.76°C to −1.62°C, with warmer temperatures in the upper 20 m of the water column (**Figure 9a**). Seawater salinity ranged from 28.2 to 30.7. From S1 to S4, the water column was well mixed, as no salinity gradient was observed

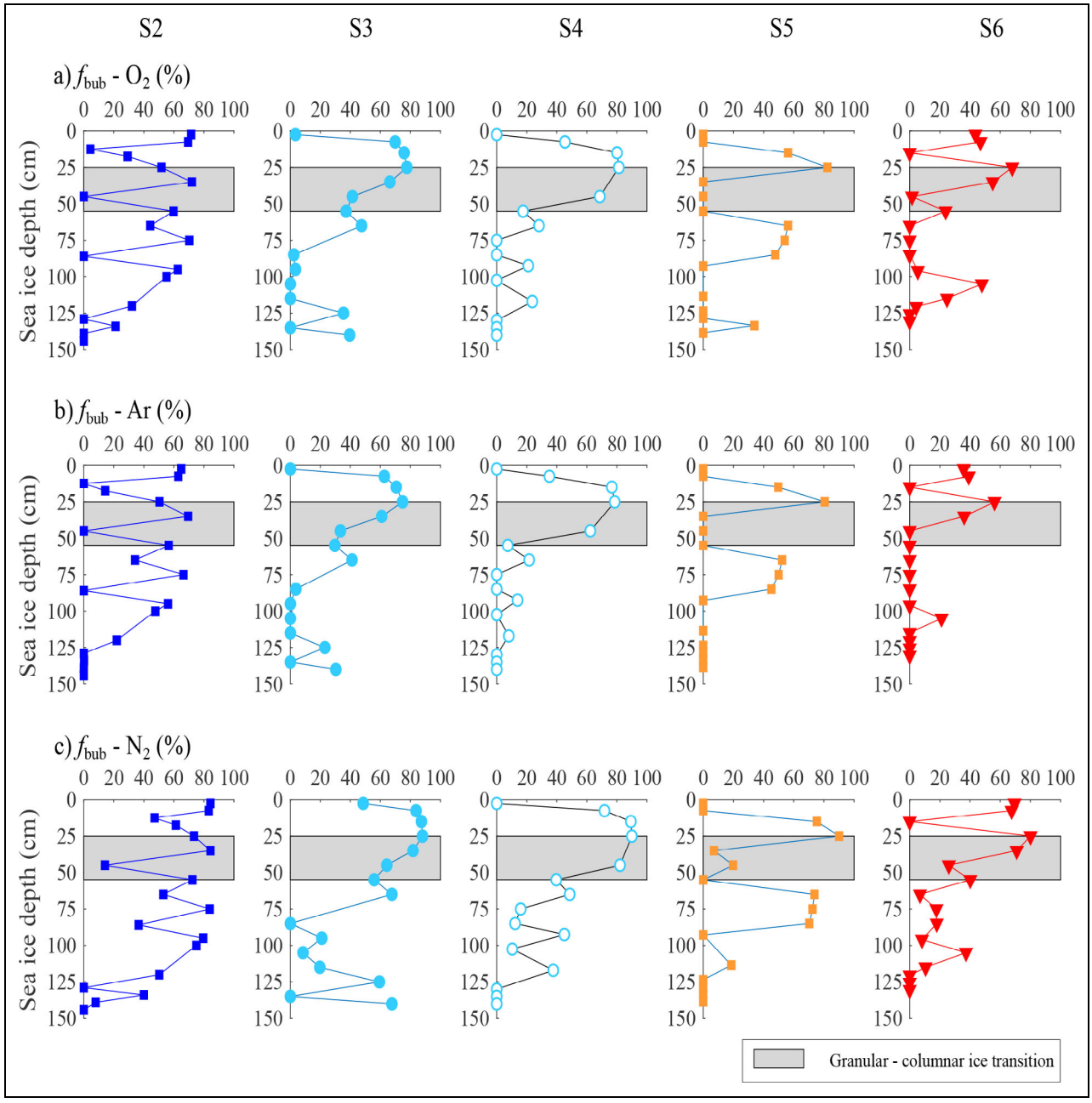

Figure 8. Gas bubble concentrations within the sea ice. Depth profiles of a) $O_{2\ (g)}$ (µmol L_{ice}^{-1}), b) $Ar_{(g)}$ (µmol L_{ice}^{-1}), and c) $N_{2\ (g)}$ (µmol L_{ice}^{-1}) as gas bubbles within sea ice. The grey area represents the granular-columnar ice transition, as defined by the $\delta^{18}O$ (**Figure 4**). S1–S6 refer to progressive sampling events over time (**Table 1**) at the sampling site (**Figure 1**).

throughout the water column. Starting on June 14 (between S4 and S5; **Table 1**), a halocline started to develop with salinity lower than 30 observed in the upper 20 m (**Figure 9b**). Seawater $\delta^{18}O$ values were slightly depleted, ranging from −2.90‰ to −0.73‰ (**Figure 9e**). The upper layer of the water column exhibited more depleted $\delta^{18}O$ values, averaging −2.1‰ (SD = 0.35, n = 21). Over the survey, surface water $\delta^{18}O$ decreased, associated with the lower sea surface salinity. TA and DIC concentrations ranged from 1965 to 2294 µmol kg^{-1} and from 1942 to 2248 µmol kg^{-1}, respectively (**Figure 9c** and **d**). Starting on June 14, a slight decrease was observed in the upper layer of the water column. Lower concentrations were observed throughout the water column on June 24.

3.4. Air–ice CO_2 exchanges

During the survey, the air–ice CO_2 fluxes averaged −0.31 mmol m^{-2} d^{-1} (SD = 0.66, n = 712) and ranged from −4.26 to 1.05 mmol m^{-2} d^{-1} (**Figure 10c**). Up to June 11 (S4), strong uptake of atmospheric CO_2, averaging −0.59 mmol m^{-2} d^{-1} (SD = 0.83, n = 337), was observed. After June 11, the overall uptake of atmospheric CO_2 decreased, averaging −0.04 mmol m^{-2} d^{-1} (SD = 0.16,

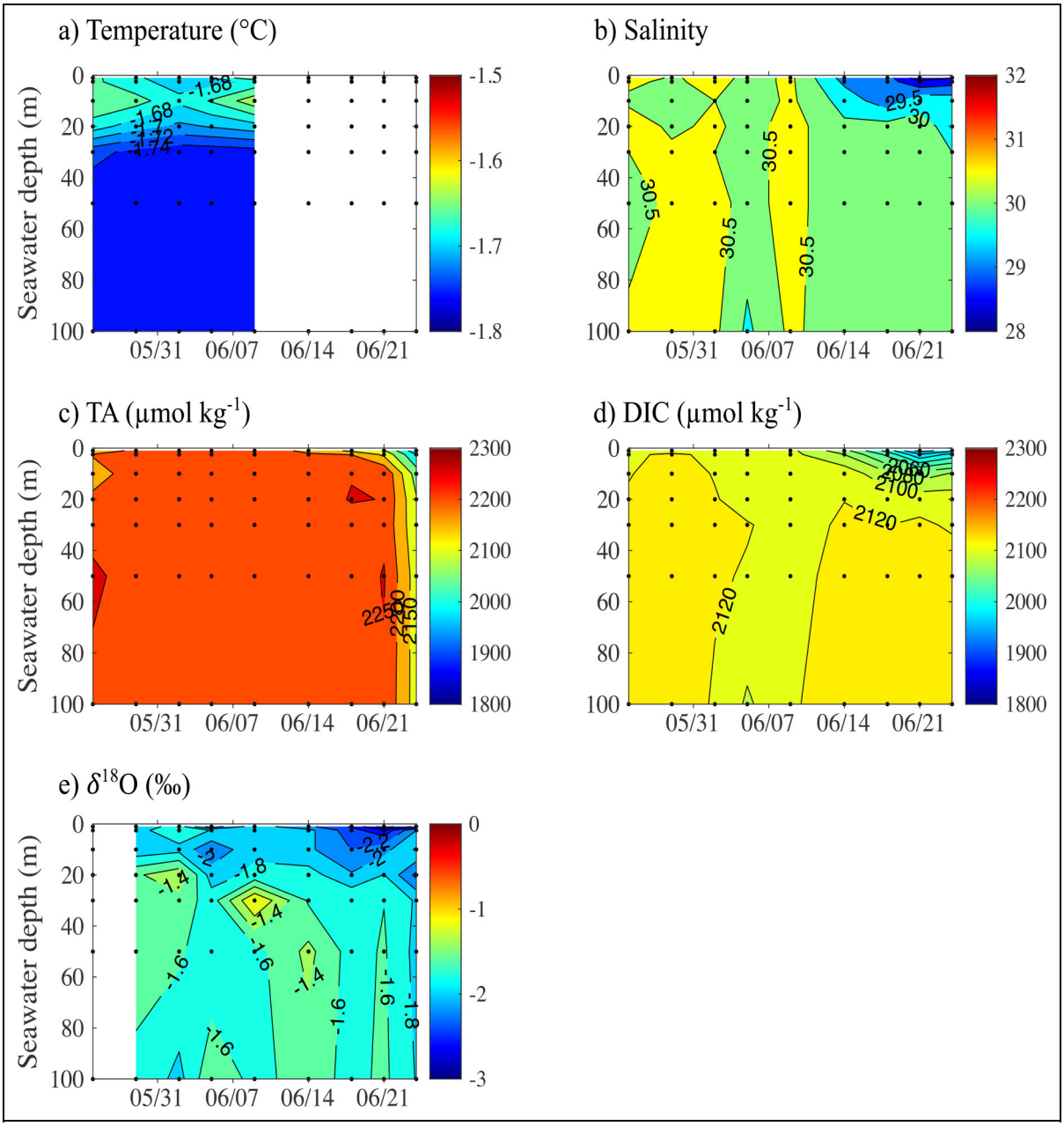

Figure 9. Seawater properties. Depth profiles over time of seawater a) temperature (°C), b) salinity, concentrations of c) total alkalinity (TA; µmol kg^{-1}) and d) dissolved inorganic carbon (DIC; µmol kg^{-1}), and e) δ^{18}O (‰). Contour plot containing the isolines of variables X based on linear regression. Seawater sampling depths are illustrated by black dots. Dates are given as month/day.

n = 352). This difference is also noticeable when fluxes are averaged for each day (**Figure 10d**). Daily averaged air–ice CO_2 fluxes ranged from −26.6 to 1.2 mmol m^{-2}. Before June 11 (S4), a large daily uptake of atmospheric CO_2 was estimated. After that, the magnitude of the air–ice CO_2 exchange decreased with a moderated release of CO_2 from the ice to the atmosphere on some occasions (June 19, 21, 24, and 25).

4. Discussion

4.1. Sea ice properties

The increase in atmospheric temperature (**Figure 10a**) led to thinning snow cover (**Figure 2**), increasing sea ice temperature (**Figure 3a**), and decreasing bulk ice salinity (**Figure 3b**). As atmospheric temperature remained above 0°C, melt ponds were observed at the ice surface (S5 and S6; **Table 1**) associated with surface ice temperature around 0°C and surface ice salinity lower than 2. Strongly depleted δ^{18}O values observed in the top 25 cm section of the ice column (**Figure 3d**) could be due to sea ice formation from already depleted surface seawater or to the contribution of meteoric ice (i.e., precipitation transformed into ice, including snow ice and/or superimposed ice formation) to the total ice thickness.

In summertime, the area is under the strong influence of surrounding glaciers, as inputs of freshwater runoff, depleted in δ^{18}O, are responsible for the large decrease in surface seawater salinity and δ^{18}O (Bendtsen et al.,

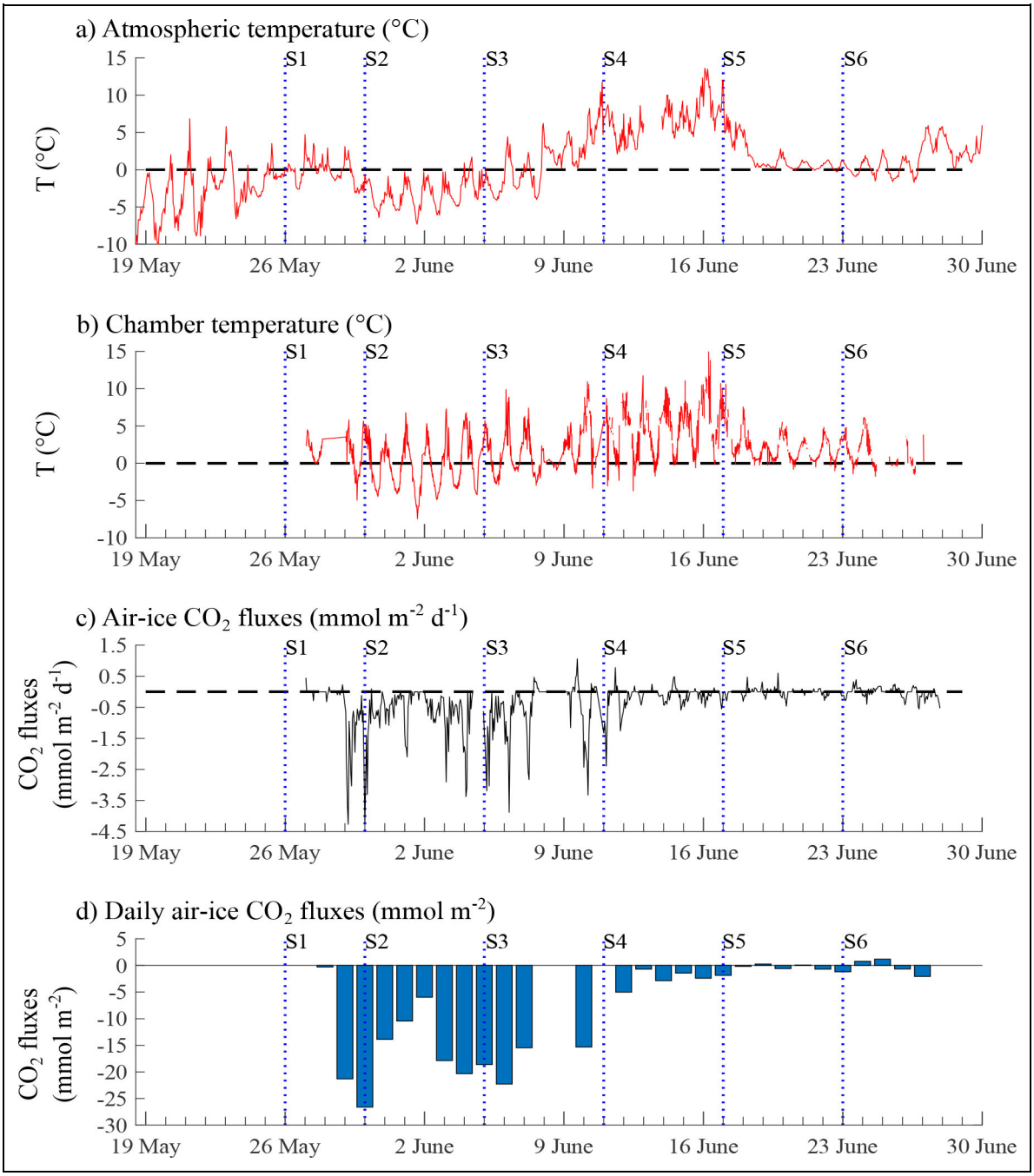

Figure 10. Changes in air temperature and air–ice CO_2 fluxes. Evolution of a) atmospheric temperature (°C) measured at 2 m and averaged every hour (data available through the Greenland Ecosystem Monitoring, GEM, programme at https://data.g-e-m.dk/, doi:10.17897/XV96-HC57), b) in-situ chamber temperature (°C), c) air–ice CO_2 fluxes (mmol m^{-2} d^{-1}), and d) daily averaged air–ice CO_2 fluxes (mmol m^{-2}). Blue dotted lines represent the sampling events (S1–S6; **Table 1**) at the sampling site (**Figure 1**).

2014), as observed during our survey starting on June 14 (**Figure 9e**). Sea ice formation from surface seawater already depleted in $\delta^{18}O$ would result in depleted $\delta^{18}O$ within sea ice (Geilfus et al., 2021). However, $\delta^{18}O$ values at or above −5‰ have been observed for surface seawater in early fall (Rysgaard, unpublished data). Sea ice formation from such fall surface seawater would not likely be responsible for the $\delta^{18}O$ values lower than −5‰ observed in the upper sea ice section of this study, especially as the freezing process potentially enriches the ice in heavy isotopes (maximum fractionation of +3‰ at low freezing rate; Souchez et al., 1988).

During our survey, sea ice was covered with 35–55 cm of snow (**Table 1**, **Figure 2**), insulating the ice from changes in atmospheric temperatures (**Figure 10a**) and thereby muting the thermal fluctuation within sea ice (Massom et al., 2001). Melting snow and meltwater refreezing at the ice surface is a well-known mechanism of ice formation (i.e., superimposed ice) during the warm season (Haas et al., 2001; Freitag and Eicken, 2003;

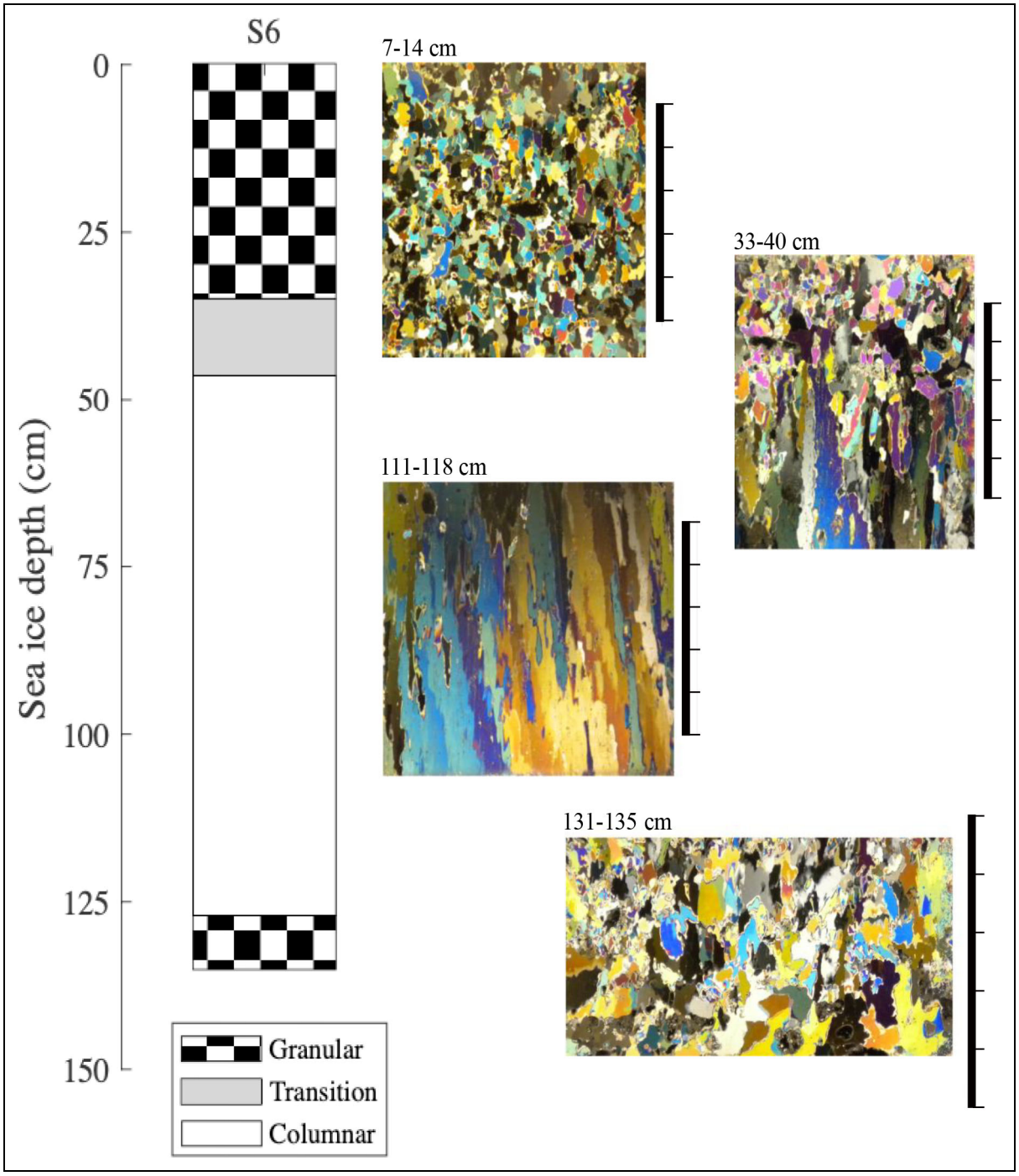

Figure 11. Sea ice microstructure. Sea ice microstructure observed in thin section via cross-polarized light at sampling event S6 (**Table 1**). A 5-cm bar scale is represented next to the pictures.

Kawamura et al., 2004). Prior to the survey, the succession of short periods with warm atmospheric temperatures (**Figure 10a**) could have initiated successive melting and refreezing cycles of snow, leading to the formation of superimposed ice. However, a layer of slush was not observed initially (**Table 1**, **Figure 2**), and the relatively warm temperature at the snow-ice interface (**Figures 2a** and **3a**) combined with the high salinity of the slush layer (**Figure 2b**) would make the formation of superimposed ice unlikely. In addition, the presence of large polygonal crystals, typical of superimposed ice (Kawamura et al., 2004), was not observed during the analysis of sea ice microstructure (**Figure 11**).

The thick snow cover also had the potential to depress the ice surface below sea level due to its own weight, as evidenced by the development of a negative freeboard (**Table 1**). This negative freeboard could result in seawater (laterally from the edge of the floe or through cracks and ridging) and/or infiltration of brine onto the ice surface, producing a layer composed of a mixture of snow and seawater and/or brine (i.e., slush). Under cold atmospheric conditions, this saline slushy layer can freeze, forming snow ice (Maksym and Jeffries, 2000). Snow ice is typically

characterized by polygonal granular ice texture, low bulk ice salinity and depleted $\delta^{18}O$ (Eicken and Lange, 1989; Lange et al., 1990). The sea ice microstructure (**Figure 11**), analyzed only for S6, highlights the presence of granular ice texture in the upper 35 cm of the ice column, followed by columnar ice towards the bottom of the ice where a thin layer of granular ice was also observed. The top 35 cm section of granular ice is associated with strongly depleted $\delta^{18}O$ values (**Figure 3d**), followed by a layer of transition between granular and columnar ice texture (35–45 cm), supporting the presence of snow ice in the upper 35 cm at S6. The transition from granular to columnar ice (from 35 cm to 50 cm depth), characterized by a steep increase in $\delta^{18}O$ values (from −5‰ to −2‰) and the presence of a local minimum in bulk salinity (**Figure 3b**), could correspond to the initial sea ice formation in the fjord from surface seawater of low salinity. Assuming the transition between granular and columnar ice and the steep increase in $\delta^{18}O$ values observed at S6 are representative of the earlier sampling events, we estimated that the snow ice contribution to total ice thickness ranged from 25% (S6) to 40% (S4; **Table 1**).

However, granular ice texture, associated with depleted $\delta^{18}O$ (−5.3‰; **Figure 3d**), was also observed in the bottom 4 cm of S6 (**Figure 11**). While sea ice microstructure analysis was not performed for S5, a depleted $\delta^{18}O$ value (−9.6‰) was also observed in the bottom sea ice layer (**Figure 3d**), suggesting that a similar process may have occurred at both S5 and S6. Depleted $\delta^{18}O$ values observed at the sea ice interface with the water column were associated with low bulk ice salinity (**Figure 3b**). Therefore, freezing of depleted $\delta^{18}O$ and low salinity water at the ice-water column interface could have resulted in the observed depleted $\delta^{18}O$ granular sea ice bottom.

Meltwater from snow or sea ice melt can drain through the sea ice matrix and accumulate below the sea ice. At the interface between this fresh water and the underlying seawater, double-diffusive convection of heat and salt occurs, leading to the formation of underwater ice, characterized by low bulk ice salinity and depleted $\delta^{18}O$ values (Martin and Kauffman, 1974; Eicken et al., 2002; Notz et al., 2003; Polashenski et al., 2012), and a granular (frazil origin) texture. This process has been suggested to be the only process by which new ice can be formed during summer (Notz et al., 2003). Alternatively, refreezing of $\delta^{18}O$-depleted river water at the ice-water column interface could also be responsible for the presence of granular ice texture associated with depleted $\delta^{18}O$ at the sea ice bottom. Starting on June 14, a decrease of both sea surface salinity and $\delta^{18}O$ was observed (**Figure 9**) associated with increasing river discharges into Tyrolerfjord. As river waters in the area have a major influence from snow and ice (from the Greenland ice sheet) melt, their $\delta^{18}O$ values must be close to the observed snow $\delta^{18}O$ (**Figure 2c**). If a thin layer of undisturbed river water (i.e., depleted in $\delta^{18}O$ freshwater) was present at the water column surface, its freezing at the contact with the sea ice bottom could be responsible for the presence of $\delta^{18}O$-depleted ice bottom layer. However, the presence of undisturbed river water below the sea ice was not observed. In addition, averaged surface seawater $\delta^{18}O$ (−2.1‰, SD = 0.3, n = 5; **Figure 9e**) suggests that a seawater contribution to the bottom granular ice layer (with $\delta^{18}O$ from −5.3‰ to −9.6‰) was unlikely. Therefore, we propose that a mixture of melt pond water (average $\delta^{18}O$ of −13.6‰, SD = 0.2, n = 2; **Figure 2c**) and sea ice meltwater, draining through the sea ice and freezing at the sea ice-water column interface was responsible for the depleted $\delta^{18}O$, low bulk salinity, and granular ice texture observed at the sea ice bottom of S5 and S6.

4.2. Gas dynamics

The observed ranges of gas concentrations are consistent with previous studies from both Arctic (Zhou et al., 2013; Crabeck et al., 2014) and Antarctic (Matsuo and Miyake, 1966; Van der Linden et al., 2020) sea ice. While O_2 and N_2 are both biogenic gases, potentially affected by both biological activity and physical processes, Ar does not have biological sources or sinks and is only affected by physical processes. Therefore, Ar can be considered an inert gas and used as a tracer of physical processes impacting gas concentration and transport within sea ice (Zhou et al., 2013; Crabeck et al., 2014). The ratio $[O_2]$:[Ar] has been used in seawater to remove the physical contribution to O_2 concentration variability and determine the biological production of O_2 (Cassar et al., 2009; Eveleth et al., 2014). It has also been used to estimate the net community production within Arctic (Zhou et al., 2014) and Antarctic sea ice (Van der Linden et al., 2020). Sea ice gas ratios were compared with the gas ratio estimated for seawater (based on averaged surface seawater temperature, −1.7°C, and salinity, 30; blue dashed line in **Figure 12**) and the atmosphere (National Oceanic and Atmospheric Administration, 1976; back dotted line in **Figure 12**). Regarding the $[O_2]$:[Ar] ratio, the abiotic range is restrained by the seawater and atmospheric $[O_2]$:[Ar] value (20.5 and 22.5, respectively). Thus, for $[O_2]$:[Ar] values falling within the abiotic range, differentiating biological from physical and chemical processes is not possible, while $[O_2]$:[Ar] outside the abiotic range could be attributed to biological activity and considered for computation of net community production.

The relative proportions of O_2, N_2, and Ar (**Figure 12b, c**, and **d**) reflect a mixed contribution of the dissolved and gaseous fractions (i.e., bubbles) of each gas within the sea ice, with a dominance of the gaseous fraction, as our observations (regression line in **Figure 12**) were closer to the atmospheric ratio (dotted line in **Figure 12**) compared to the seawater ratio (dashed line in **Figure 12**). In addition, the estimated bubble fraction (Equation 3, **Figure 8**) suggests that up to 80% of the gas species were in the gas phase, while less than 20% were dissolved in the brine. This difference between gas and dissolved phase is consistent with gas observations previously reported in sea ice from Antarctica (Matsuo and Miyake, 1966), an Arctic fjord (Crabeck et al., 2014), and an artificial sea ice mesocosm (Tison et al., 2002). In this study, $[O_2]$ and $[N_2]$ correlated strongly with [Ar] (R^2 = 0.99 and 0.98, respectively; **Figure 12**), suggesting that physical processes mainly controlled the gas composition within sea ice,

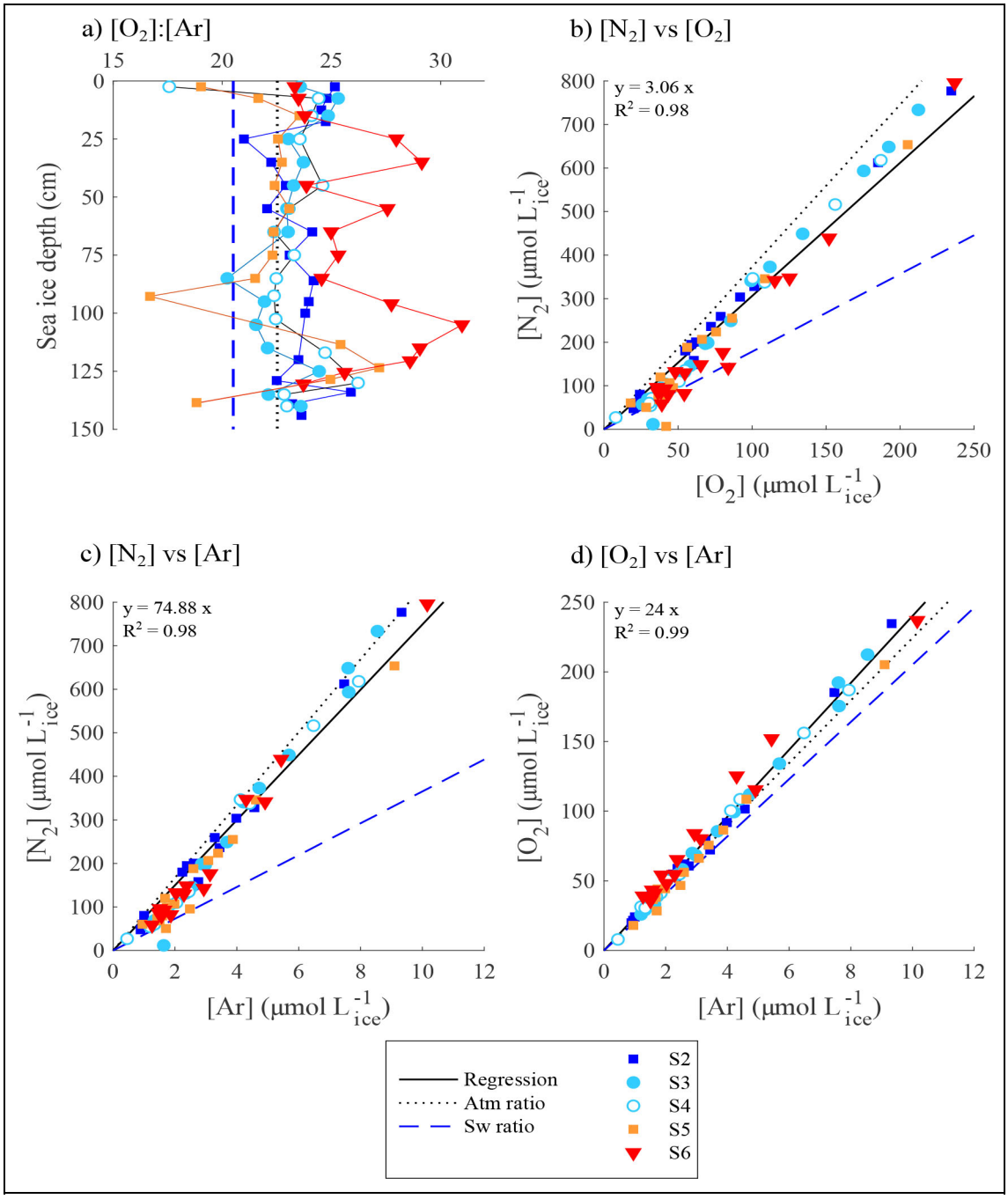

Figure 12. Gas ratio profiles and relationships. Panel a) presents depth profiles of the O_2:Ar ratio within the sea ice, followed by the relationships between b) $[N_2]$ and $[O_2]$, c) $[N_2]$ and [Ar], and d) $[O_2]$ and [Ar] within the ice. The solid line in b)–d) is the regression line (equation and R^2 shown in panels), the blue dashed line represents the respective ratios in seawater (Sw; based on averaged surface seawater salinity of 30 and temperature of −1.7°C), and the dotted black line is the respective ratio in the atmosphere (Atm). S1–S6 refer to progressive sampling events over time (**Table 1**) at the sampling site (**Figure 1**).

while biological processes had only a minor effect. However, literature record values of $[O_2]$:[Ar] as high as 31, well above the abiotic range, were observed at S6 (**Figure 12a**), suggesting a significant contribution of biological processes, as discussed later.

Maximum gas concentration (**Figure 6**) and gas content as bubbles (**Figure 8**) appear to be centred at 25 cm depth in the sea ice. This depth coincides with the granular–columnar ice transition and the presence of snow ice in the upper sea ice layer (**Figure 11**). At that depth, about 80% of the gas species were in the gas phase while less than 20% were dissolved in the brine. Snow ice and granular ice have been reported to contain more bubbles compared to columnar ice (Crabeck et al., 2016). The gas peak decreased over time, with minimum concentrations observed at the sea ice surface, suggesting a release of gas towards the atmosphere. Gas bubbles released to the atmosphere result in gas concentrations reaching the

atmospheric saturation (as at S3 in **Figure 7**). However, surface sea ice was far below atmospheric saturation in gases in S4 and S5 (**Figure 7**) when atmospheric temperatures increased and remained above 0°C (**Figure 10a**), leading to the formation of melt ponds. The refreezing of meltwater, already depleted in gases (Glud et al., 2002; Rysgaard and Glud, 2004), will release gases towards the atmosphere, resulting in an ice layer largely depleted in gas. However, the presence of superimposed ice, formed from refrozen snow meltwater at the sea ice surface, was not observed during the thin section analysis at S6 (**Figure 11**). Alternatively, meltwater has been suggested to refreeze as it intrudes into brine-filled pore structures within the ice to form interposed ice plugs (Freitag and Eicken, 2003; Polashenski et al., 2012), resulting in a surface ice layer strongly depleted in gas (**Figures 6** and **7**). At S6, gas concentrations in the surface ice layer increased above the atmospheric saturation. At the time, melt ponds were completely developed and sea ice cores were extracted from the "dry ice," usually referred to as "white ice" due to its high reflectance (Greenfell and Maykut, 1977; Perovich, 1996), located next to the melt ponds. As a result of melt pond formation, meltwater is drained from the upper layer of the white ice, leaving the drained ice surface with a high content of air inclusions (Perovich, 1996). Therefore, the upper sea ice section exhibited similar gas ratios (i.e., O_2:Ar) as the atmosphere (**Figure 12**) and concentrations above gas saturation due to the fact that the latter refers to a maximum dissolved concentration in the brines, lacking the impact of "air spaces" in the "rotten" surface ice.

In the sea ice interior, gas concentrations were close to, or below, atmospheric saturation (**Figure 6**), suggesting that gas incorporation at the ice-seawater interface occurred close to the atmospheric solubility (Zhou et al., 2013; Crabeck et al., 2014), while brine drainage could also have contributed to lowering the gas concentration. However, gas concentrations at the ice bottom of S5 and S6 were much lower than atmospheric saturation. These ice sections, characterized by depleted $\delta^{18}O$ (**Figure 3**) and granular ice texture (**Figure 11**), are suggested to have formed by refreezing meltwater. Sea ice meltwater is undersaturated in O_2 (Glud et al., 2002); assuming that O_2, Ar, and N_2 behave in the same way (Rysgaard and Glud, 2004), the refreezing of meltwater, depleted in gases, will contribute to the undersaturation observed at the sea ice bottom. However, we cannot rule out partial gas losses during core extraction.

In order to estimate the sea ice net community production, we first estimated the impact of physical processes on the O_2 concentration ($[O_2]_{phys}$; Equation 6, **Figure 13b**), then the O_2 concentration associated with biological activity ($[O_2]_{bio}$; Equation 7, **Figure 13c**). While the observed $[O_2]$ ranged from 1 to 237 μmol L_{ice}^{-1} (averaging 73 μmol L_{ice}^{-1}, SD = 54, n = 73; **Figures 7a** and **13a**), $[O_2]_{phys}$ and $[O_2]_{bio}$ ranged from 2.7 to 208 (average: 62, SD = 45, n = 80) and from 6.5 to 44 μmol L_{ice}^{-1} (average: 10.5, SD = 10.3, n = 80, **Figure 13**), respectively, with maximum O_2 observed in the upper 25 cm of the ice column. Note that $[O_2]_{bio}$ values are well above the measurement uncertainties for both O_2 and Ar (<1%; see Methods), revealing a clear signal. However, overall, the relative contribution of $[O_2]_{bio}$ to the O_2 pool appears to be minor compared to $[O_2]_{phys}$, with estimated values ranging from −0.2 to 0.3 (**Figure 13d**). Nevertheless, increases in $[O_2]_{bio}$ contributions were observed at S6, with maximum $[O_2]_{bio}$:$[O_2]$ values in accordance with the high $[O_2]$:[Ar] ratio in S6 (**Figure 12a**).

Sea ice NCP assessments (in μmol L_{ice}^{-1} d^{-1}; **Figure 13e**) are given for the upper 25 cm of the ice (noted surface), bottom 15 cm layer (noted bottom), and the sea ice interior (noted interior). Positive NCP values indicate an O_2 production (equivalent to an inorganic carbon uptake, i.e. autotrophy), while negative values correspond to O_2 consumption (equivalent to inorganic carbon production, i.e., heterotrophy). The range of NCP values estimated in this study (from −2.25 to 2.6 μmol $L_{ice}^{-1}d^{-1}$) fall within previous estimates for sea ice derived from $[O_2]$:[Ar] ratios (Zhou et al., 2014; Van der Linden et al., 2020) or from oxygen incubations (Søgaard et al., 2010; Campbell et al., 2017). Early in the survey (S2 and S3), NCP exhibited positive values, indicating net autotrophy (**Figure 13**). From S3 to S5, NCP values became negative, indicating that heterotrophy dominated. At the end of the survey (S5 and S6), sea ice became autotrophic again. Heterotrophy within sea ice has been previously reported in Young Sound, where an O_2 consumption up to 13 μmol L_{ice}^{-1} d^{-1} was estimated (Rysgaard and Glud, 2004), as well as in landfast sea ice in Franklin Bay (Canadian Arctic), with an estimated O_2 consumption of 3 μmol L_{ice}^{-1} d^{-1} (Rysgaard et al., 2008). The increase in the $[O_2]_{bio}$ contribution to the overall pool of O_2 (**Figure 13d**) associated with positive estimates of NCP (**Figure 13e**) indicates that sea ice was net autotrophic from S5 to S6. If both Chl-*a* and nutrient concentrations were low (**Figure 4**), suggesting a low sea ice algal productivity during the study period, a slight (though up to 4-fold in the areas of high O_2:Ar) increase of Chl-*a* was observed in S5 associated with an increase of NO_3^-, potentially increasing $[O_2]_{bio}$. Its rapid degradation would have led to the increase of PO_4^{3-} observed in S6. Therefore, the strong correlations between $[O_2]$, $[N_2]$, and [Ar] (**Figure 12**), associated with the minor contribution of $[O_2]_{bio}$ to the overall pool of O_2 (**Figure 13d**), suggest that gas composition within sea ice is mainly controlled by physical processes, but with a minor and clearly discernible contribution of biological processes.

4.3. The carbonate system

Most of the changes in TA and DIC observed within sea ice appeared to be driven mainly by salinity changes (**Figure 5c** and **f**). However, a fair number of data points from S1 exhibited lower/higher TA and DIC than expected from salinity changes. Data points with higher-than-expected TA and DIC (**Figure 5c** and **f**) correspond to data with *n*TA and *n*DIC >400 μmol kg^{-1} (**Figure 5b** and **e**), aligned with the theoretical trend of calcium carbonate dissolution (**Figure 5h**). Conversely, data points with lower-than-expected TA and DIC (**Figure 5c** and **f**) correspond to data with *n*TA and *n*DIC <300 μmol kg^{-1} (**Figure 5b** and **e**),

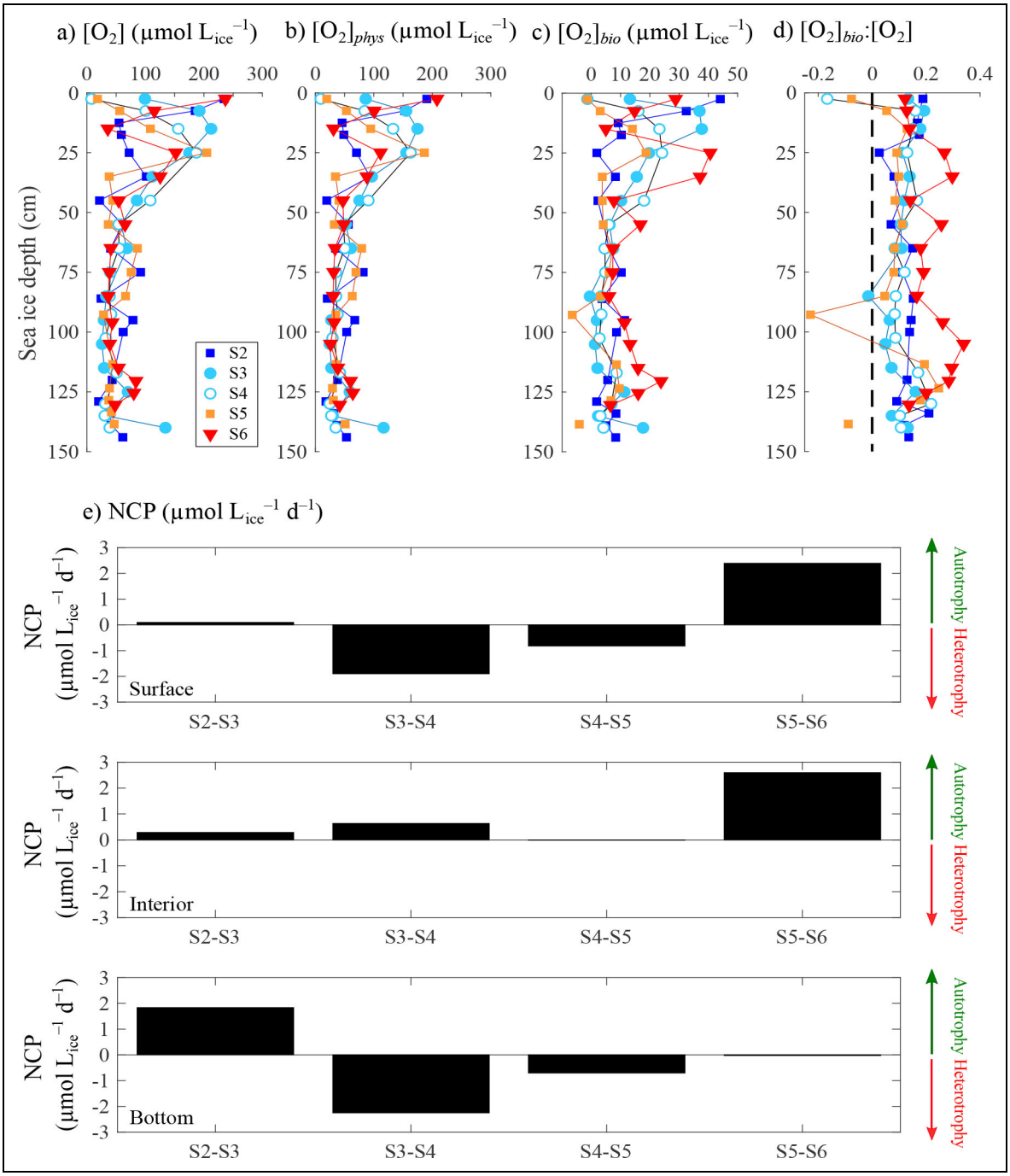

Figure 13. Oxygen concentrations and net community production in the sea ice. Depth profiles of a) O_2 concentrations within bulk ice ([O_2] in µmol L_{ice}^{-1}), b) O_2 concentrations due to physical processes ([O_2]*phys* in µmol L_{ice}^{-1}), c) O_2 concentrations associated with biological activities ([O_2]*bio*), and d) the ratio [O_2]*bio*:[O_2] in the sea ice. Panel e) represents the sea ice net community production (NCP in µmol L_{ice}^{-1} d^{-1}) estimated for the upper 25 cm layer (surface), bottom 15 cm layer (bottom) and the sea ice interior (interior). S1–S6 refer to progressive sampling events over time (**Table 1**) at the sampling site (**Figure 1**).

aligned with the theoretical trend of calcium carbonate precipitation (**Figure 5h**). These patterns suggest that precipitates of calcium carbonate were present within the sea ice at S1 and started to dissolve in the upper and bottom layers of the ice as the ice warmed. While the presence of calcium carbonate precipitates (such as ikaite, $CaCO_3 \bullet 6H_2O$) within sea ice was not observed during this survey, the area is known to support ikaite precipitation (Rysgaard et al., 2007), with estimates of ikaite precipitation in surface sea ice up to 900 µmol kg^{-1} (Rysgaard et al., 2013). From S2 onwards, most of the sea ice data fall along the calcium carbonate dissolution line, with a slight offset toward CO_2 uptake and/or respiration (**Figure 5h**). Where the sea ice uptake of atmospheric CO_2 has been quantified (**Figure 10c** and **d**), the impact of biology may be minor overall, but is noticeable for S6 (**Figures 12** and **13**).

4.4. Air—ice CO_2 fluxes

Air–ice CO_2 fluxes mainly depend on sea ice permeability and the CO_2 concentration gradient between the atmosphere and the ice surface (i.e., brine and meltwater, including slush and melt ponds). While brine volume calculations (**Figure 3c**) confirmed that sea ice was permeable to gas exchanges (Golden et al., 2007; Zhou et al., 2013), slush, brine, and melt ponds were all undersaturated in CO_2 compared to the atmosphere (**Figures 2j** and **6g**), supporting the overall uptake of atmospheric CO_2 by the snow-covered sea ice (**Figure 10c** and **d**).

The air temperature and its impacts on the surface ice layer strongly affected the air–ice CO_2 exchanges. During most of the survey, a diurnal pattern of CO_2 fluxes can be observed, with stronger uptake of atmospheric CO_2 occurring when the chamber temperature rose to about 0°C as the air temperature increased during daylight. At nighttime, as atmospheric and chamber temperatures decreased, the air-ice exchanges of CO_2 weakened, with a slight release of CO_2 from the ice to the atmosphere on a few occasions (**Figure 10c**). Increasing air temperature initiated the snow melt and the formation of a slush layer at the snow-ice interface with the atmosphere (**Figure 2**). The input of snow meltwater into the slush resulted in decreasing slush salinity and pCO_2 (**Figure 2j**), supporting the uptake of atmospheric CO_2 by the snow-covered sea ice. The nocturnal refreezing of the slush layer and surface ice reduced the exchanges of CO_2 with the atmosphere and episodically induced a CO_2 release to the atmosphere, like the release of CO_2 to the atmosphere by young growing sea ice (Geilfus et al., 2013; Fransson et al., 2015). Similar patterns have been reported over landfast sea ice using both the chambers (Van der Linden et al., 2020) and eddy covariance technique (Papakyriakou and Miller, 2011).

Due to slush and sea ice brine undersaturation in CO_2 (**Figures 2j** and **5g**), compared to the atmosphere, the snow-covered sea ice acted as a sink for atmospheric CO_2, with uptake up to -4.26 mmol m^{-2} d^{-1} observed from S1 to S4 (up to June 11; **Figure 10c**). However, as the air temperature remained above 0°C (June 11) and slush and brine pCO_2 reached their minima, the overall uptake of atmospheric CO_2 weakened (averaging -0.04 mmol m^{-2} d^{-1}; **Figure 10c**). On June 12, meltwater began to accumulate at the sea ice surface, forming melt ponds. Therefore, to endure the air–ice CO_2 flux measurements, chambers were installed on the remaining sea ice from which the meltwater had drained from the surface elevation into the melt ponds, the so-called white ice (Perovich, 1996). As the upper layer of the white ice is depleted of liquid (brine and/or meltwater) and has a high content of air inclusions (Perovich, 1996), its ability to exchange CO_2 is reduced, leading to a weakening of the measured uptake of atmospheric CO_2 by the chambers. Therefore, the values obtained on white ice may not be representative for the actual uptake of atmospheric CO_2 by both melt ponds and sea ice.

Overall, the CO_2 fluxes reported in this study are in the same range as in previous studies, both Arctic and Antarctic, using a similar system (Geilfus et al., 2012; Nomura et al., 2013; Delille et al., 2014; Brown et al., 2015; Geilfus et al., 2015; Van der Linden et al., 2020). The decreasing uptake of CO_2 as melt ponds developed was also reported by Geilfus et al. (2015). However, this decrease was observed mainly over melt ponds and was attributed to the decreasing pCO_2 gradient between melt ponds and the atmosphere as melt ponds tend to reach equilibrium with the atmosphere over time (Geilfus et al., 2015). In this study, the sea ice uptake of atmosphere CO_2 weakened before melt pond formation, probably due to the decreasing amount of brine and meltwater contained in the ice as it is drained from the upper ice layer, either vertically through the ice thickness or horizontally to form the melt ponds.

5. Conclusions

During the spring–summer transition at our North Greenland Arctic fjord location, the increase in air temperature led to the formation of melt ponds, resulting in significant changes in sea ice physical properties, gas composition, and the ability of sea ice to take up atmospheric CO_2. Physical processes mainly controlled the gas composition, while the impact of biological processes was noticeable at the end of the survey (S5 and S6; **Figures 12** and **13**). Maximum gas concentrations and bubble content were observed in the upper sea ice sections, with the surface sea ice concentration decreasing over time due to the release of gas to the atmosphere. At the sea ice interface with the atmosphere, the accumulation of meltwater into melt ponds was associated with the formation of interposed ice, where meltwater refreezes as it intrudes into the brine-filled pore structure, forming ice plugs (Freitag and Eicken, 2003; Polashenski et al., 2012). As meltwater drained throughout the ice column and accumulated at the sea ice bottom, it refroze forming a layer of underwater ice (Martin and Kauffman, 1974; Eicken et al., 2002; Notz et al., 2003; Polashenski et al., 2012). In both cases, ice formation from meltwater already depleted in gas resulted in ice strongly depleted in gas, first at the ice surface during early melt pond formation, then at the sea ice bottom (**Figures 6** and **7**).

Due to the increasing sea ice temperature, brine freshening, and ikaite dissolution, the sea ice was mainly undersaturated in CO_2 compared to the atmosphere (**Figure 5**), resulting in the uptake of atmospheric CO_2 (**Figure 10**). However, as melt ponds formed, the remaining ice surface (the "white ice") became depleted in water as brine and meltwater drained and accumulated into melt ponds. Therefore, even though the sea ice was strongly undersaturated in CO_2 compared to the atmosphere, it could not exchange CO_2 with the atmosphere, resulting in a weakening uptake of atmospheric CO_2. This study illustrates the important role of melt pond formation and dynamics in controlling the physical properties and gas composition of sea ice, with strong consequences for sea ice uptake of atmospheric CO_2.

Data accessibility statement

Data are available at Geilfus, N. (2022). Daneborg–Young Sound 2014, HydroShare, https://doi.org/10.4211/hs.

a3c0d38322fc46ea96ecea2438b29283. Air temperature data (**Figure 10a**) are accessible at https://data.g-e-m.dk/, doi:10.17897/XV96-HC57.

Acknowledgments

We gratefully acknowledge the contributions of the Canada Excellence Research Chair (CERC) and Canada Research Chair (CRC) programs. Support was also provided by the Natural Sciences and Engineering Research (NSERC) Council, the Canada Foundation for Innovation and the University of Manitoba. We wish to thank the entire team behind the Daneborg Research Station, managed by Aarhus University. This work is a contribution to the ArcticNet Networks of Centres of Excellence and the Arctic Science Partnership (ASP) asp-net.org. BD is a research associate of the F.R.S-FNR. The authors are in debt to Marie Kotovitch, Odile Crabeck, and Egon Frandsen for their technical assistance in the field experiment and subsequent analysis.

Funding

Financial support for this study was provided by the Canada Excellence Research Chairs program, the Canada Research Chairs program, the Natural Sciences and Engineering Research Council, and the Canada Foundation for Innovation, the Belgian Science Policy (project Bigsouth, SD/CA/05A) and the Fonds National de la Recherche Scientifique (F.R.S-FNRS). BD is a Research Associate of the FRS-FNRS.

Competing interests

The authors declare no competing interests.

Author contributions

Field sampling was performed by N-XG and BD, laboratory and data analyses were performed by N-XG, ML, BD, and J-LT, and the manuscript was written and edited by N-XG, BD, ML, J-LT, and SR. All authors approved the submission of this manuscript.

References

Alkire, MB, **Nilsen, F**, **Falck, E**, **Søreide, J**, **Gabrielsen, TM.** 2015. Tracing sources of freshwater contributions to first-year sea ice in Svalbard fjords. *Continental Shelf Research* **101**: 85–97. DOI: https://doi.org/10.1016/j.csr.2015.04.003.

American Public Health Association. 1998. *Standard methods for the examination of water and wastewater*. Washington, DC: American Public Health Association.

Bates, NR, **Mathis, JT.** 2009. The Arctic Ocean marine carbon cycle: Evaluation of air–sea CO_2 exchanges, ocean acidification impacts and potential feedbacks. *Biogeosciences* **6**(11): 2433–2459. DOI: http://dx.doi.org/10.5194/bg-6-2433-2009.

Bendtsen, J, **Mortensen, J**, **Rysgaard, S.** 2014. Seasonal surface layer dynamics and sensitivity to runoff in a high Arctic fjord (Young Sound/Tyrolerfjord, 74°N). *Journal of Geophysical Research: Oceans* **119**(9): 6461–6478. DOI: http://dx.doi.org/10.1002/2014JC010077.

Brown, KA, **Miller, LA**, **Mundy, CJ**, **Papakyriakou, TN**, **Francois, R**, **Gosselin, M**, **Carnat, G**, **Swystun, K**, **Tortell, PD.** 2015. Inorganic carbon system dynamics in landfast Arctic sea ice during the early-melt period. *Journal of Geophysical Research: Oceans* **120**(5): 3542–3566. DOI: http://dx.doi.org/10.1002/2014JC010620.

Campbell, K, **Mundy, CJ**, **Gosselin, M**, **Landy, JC**, **Delaforge, A**, **Rysgaard, S.** 2017. Net community production in the bottom of first-year sea ice over the Arctic spring bloom. *Geophysical Research Letters* **44**(17): 8971–8978. DOI: http://dx.doi.org/10.1002/2017GL074602.

Cassar, N, **Barnett, BA**, **Bender, ML**, **Kaiser, J**, **Hamme, RC**, **Tilbrook, B.** 2009. Continuous high-frequency dissolved O_2/Ar measurements by equilibrator inlet mass spectrometry. *Analytical Chemistry* **81**(5): 1855–1864. DOI: http://dx.doi.org/10.1021/ac802300u.

Chen, B, **Cai, W-J**, **Chen, L**. 2015. The marine carbonate system of the Arctic Ocean: Assessment of internal consistency and sampling considerations, summer 2010. *Marine Chemistry* **176**: 174–188. DOI: https://doi.org/10.1016/j.marchem.2015.09.007.

Cox, GFN, **Weeks, WF.** 1983. Equations for determining the gas and brine volumes in sea-ice samples. *Journal of Glaciology* **29**(102): 306–316. DOI: http://dx.doi.org/10.3189/S0022143000008364.

Crabeck, O, **Delille, B**, **Rysgaard, S**, **Thomas, DN**, **Geilfus, NX**, **Else, B**, **Tison, JL.** 2014. First "in situ" determination of gas transport coefficients (DO_2, DAr, and DN_2) from bulk gas concentration measurements (O_2, N_2, Ar) in natural sea ice. *Journal of Geophysical Research: Oceans* **119**(10): 6655–6668. DOI: http://dx.doi.org/10.1002/2014JC009849.

Crabeck, O, **Galley, R**, **Delille, B**, **Else, B**, **Geilfus, NX**, **Lemes, M**, **Des Roches, M**, **Francus, P**, **Tison, JL**, **Rysgaard, S.** 2016. Imaging air volume fraction in sea ice using non-destructive X-ray tomography. *The Cryosphere* **10**(3): 1125–1145. DOI: http://dx.doi.org/10.5194/tc-10-1125-2016.

Crabeck, O, **Galley, RJ**, **Mercury, L**, **Delille, B**, **Tison, JL**, **Rysgaard, S.** 2019. Evidence of freezing pressure in sea ice discrete brine inclusions and its impact on aqueous-gaseous equilibrium. *Journal of Geophysical Research: Oceans* **124**: 1660–1678. DOI: http://dx.doi.org/10.1029/2018JC014597.

Craig, H, **Gordon, LI.** 1965. Deuterium and oxygen-18 variations in the ocean and marine atmosphere, in Tongiorgi, E ed., *Stable isotopes in oceanographic studies and paleotemperatures*. Spoleto, Italy: Consiglio nazionale delle richerche, Laboratorio di geologia nucleare: 9–130.

Dansgaard, W, **Tauber, H.** 1969. Glacier oxygen-18 content and Pleistocene ocean temperatures. *Science* **166**(3904): 499–502. DOI: https://www.science.org/doi/10.1126/science.166.3904.499.

Delille, B, **Vancoppenolle, M**, **Geilfus, NX**, **Tilbrook, B**, **Lannuzel, D**, **Schoemann, V**, **Becquevort, S**, **Carnat, G**, **Delille, D**, **Lancelot, C**, **Chou, L**,

Dieckmann, GS, **Tison, JL.** 2014. Southern Ocean CO_2 sink: The contribution of the sea ice. *Journal of Geophysical Research: Oceans* **119**(9): 6340–6355. DOI: http://dx.doi.org/10.1002/2014JC009941.

Dickson, AG, **Millero, FJ.** 1987. A comparison of the equilibrium constants for the dissociation of carbonic acid in seawater media. *Deep Sea Research Part A. Oceanographic Research Papers* **10**(34): 1733–1743. DOI: http://dx.doi.org/10.1016/0198-0149(87)90021-5.

Dieckmann, GS, **Nehrke, G**, **Papadimitriou, S**, **Gottlicher, J**, **Steininger, R**, **Kennedy, H**, **Wolf-Gladrow, D**, **Thomas, DN.** 2008. Calcium carbonate as ikaite crystals in Antarctic sea ice. *Geophysical Research Letters* **35**(8): L08501. DOI: http://dx.doi.org/10.1029/2008GL033540.

Dmitrenko, IA, **Kirillov, SA**, **Rysgaard, S**, **Barber, DG**, **Babb, DG**, **Pedersen, LT**, **Koldunov, NV**, **Boone, W**, **Crabeck, O**, **Mortensen, J.** 2015. Polynya impacts on water properties in a Northeast Greenland fjord. *Estuarine, Coastal and Shelf Science* **153**: 10–17. DOI: http://dx.doi.org/10.1016/j.ecss.2014.11.027.

Eicken, H. 1992. Salinity profiles of Antarctic sea ice: Field data and model results. *Journal of Geophysical Research: Oceans* **97**(C10): 15545–15557. DOI: http://dx.doi.org/10.1029/92JC01588.

Eicken, H. 2003. From the microscopic, to the macroscopic, to the regional scale: Growth, microstructure and properties of sea ice, in Thomas, DN ed., *Sea ice*. London, UK: John Wiley, Blackwell Science: 22–81. DOI: http://dx.doi.org/10.1002/9780470757161.ch2.

Eicken, H, **Krouse, HR**, **Kadko, D**, **Perovich, DK.** 2002. Tracer studies of pathways and rates of meltwater transport through Arctic summer sea ice. *Journal of Geophysical Research: Oceans* **107**(C10): 8046. DOI: http://dx.doi.org/10.1029/2000JC000583.

Eicken, H, **Lange, MA.** 1989. Development and properties of sea ice in the coastal regime of the Southeastern Weddell Sea. *Journal of Geophysical Research: Oceans* **94**(C6): 8193–8206. DOI: http://dx.doi.org/10.1029/JC094iC06p08193.

Eicken, H, **Lange, MA**, **Dieckmann, GS.** 1991. Spatial variability of sea ice properties in the Northwestern Weddell Sea. *Journal of Geophysical Research: Oceans* **96**(C6): 10603–10615. DOI: http://dx.doi.org/10.1029/91JC00456.

Eveleth, R, **Timmermans, ML**, **Cassar, N.** 2014. Physical and biological controls on oxygen saturation variability in the upper Arctic Ocean. *Journal of Geophysical Research: Oceans* **119**(11): 7420–7432. DOI: http://dx.doi.org/10.1002/2014JC009816.

Fetterer, F, **Untersteiner, N.** 1998. Observations of melt ponds on Arctic sea ice. *Journal of Geophysical Research: Oceans* **103**(C11): 24821–24835. DOI: http://dx.doi.org/10.1029/98JC02034.

Fransson, A, **Chierici, M**, **Abrahamsson, K**, **Andersson, M**, **Granfors, A**, **Gårdfeldt, K**, **Torstensson, A**, **Wulff, A.** 2015. CO_2-system development in young sea ice and CO_2 gas exchange at the ice/air interface mediated by brine and frost flowers in Kongsfjorden, Spitsbergen. *Annal of Glaciology* **56**(69): 245–257. DOI: http://dx.doi.org/10.3189/2015AoG69A563.

Freitag, J, **Eicken, H.** 2003. Meltwater circulation and permeability of Arctic summer sea ice derived from hydrological field experiments. *Journal of Glaciology* **49**(166): 349–358. DOI: http://dx.doi.org/10.3189/172756503781830601.

Garcia, HE, **Gordon, LI.** 1992. Oxygen solubility in seawater: Better fitting equations. *Limnology and Oceanography* **37**(6): 1307–1312. DOI: http://dx.doi.org/10.4319/lo.1992.37.6.1307.

Geilfus, NX, **Carnat, G**, **Dieckmann, GS**, **Halden, N**, **Nehrke, G**, **Papakyriakou, TN**, **Tison, JL**, **Delille, B.** 2013. First estimates of the contribution of $CaCO_3$ precipitation to the release of CO_2 to the atmosphere during young sea ice growth. *Journal of Geophysical Research: Oceans* **118**: 244–255. DOI: http://dx.doi.org/10.1029/2012JC007980.

Geilfus, NX, **Carnat, G**, **Papakyriakou, T**, **Tison, JL**, **Else, B**, **Thomas, H**, **Shadwick, E**, **Delille, B.** 2012. Dynamics of pCO_2 and related air–ice CO_2 fluxes in the Arctic coastal zone (Amundsen Gulf, Beaufort Sea). *Journal of Geophysical Research: Oceans* **117**(C9). DOI: http://dx.doi.org/10.1029/2011JC007118.

Geilfus, NX, **Galley, RJ**, **Crabeck, O**, **Papakyriakou, T**, **Landy, J**, **Tison, JL**, **Rysgaard, S.** 2015. Inorganic carbon dynamics of melt-pond-covered first-year sea ice in the Canadian Arctic. *Biogeosciences* **12**(6): 2047–2061. DOI: http://dx.doi.org/10.5194/bg-12-2047-2015.

Geilfus, NX, **Munson, KM**, **Lemes, M**, **Wang, F**, **Tison, JL**, **Rysgaard, S.** 2021. Meteoric water contribution to sea ice formation and its control of the surface water carbonate cycle in the Wandel Sea shelf, northeastern Greenland. *Elementa: Science of the Anthropocene* **9**: 1. DOI: http://dx.doi.org/10.1525/elementa.2021.00004.

Geilfus, NX, **Tison, JL**, **Ackley, SF**, **Galley, RJ**, **Rysgaard, S**, **Miller, LA**, **Delille, B.** 2014. Sea ice pCO_2 dynamics and air–ice CO_2 fluxes during the Sea Ice Mass Balance in the Antarctic (SIMBA) experiment—Bellingshausen Sea, Antarctica. *The Cryosphere* **8**(6): 2395–2407. DOI: http://dx.doi.org/10.5194/tc-8-2395-2014.

Glud, RN, **Rysgaard, S**, **Kuhl, M.** 2002. A laboratory study on O_2 dynamics and photosynthesis in ice algal communities: Quantification by microsensors, O_2 exchange rates, ^{14}C incubations and a PAM fluorometer. *Aquatic Microbial Ecology* **27**(3): 301–311. DOI: http://dx.doi.org/10.3354/ame027301.

Golden, KM, **Eicken, H**, **Heaton, AL**, **Miner, J**, **Pringle, DJ**, **Zhu, J.** 2007. Thermal evolution of permeability and microstructure in sea ice. *Geophysical Research Letters* **34**(L16501). DOI: http://dx.doi.org/10.1029/2007GL030447.

Gosink, TA, **Pearson, JG**, **Kelly, JJ.** 1976. Gas movement through sea ice. *Nature* **263**: 41–42. DOI: http://dx.doi.org/10.1038/263041a0.

Gran, G. 1952. Determination of the equivalence point in potentiometric titration. *Analyst Part II* (**77**): 661–671. DOI: http://dx.doi.org/10.1039/AN9527700661.

Grasshoff, K, **Ehrhardt, M**, **Kremling, K.** 1983. *Methods of sea water analysis*. Deerfield Beach, FL: Verlag Chemie.

Grenfell, TC, **Maykut, GA.** 1977. The optical properties of ice and snow in the arctic basin. *Journal of Glaciology* **18**(80): 445–463. DOI: http://dx.doi.org/10.3189/S0022143000021122.

Haas, C, **Thomas, DN**, **Bareiss, J.** 2001. Surface properties and processes of perennial Antarctic sea ice in summer. *Journal of Glaciology* **47**(159): 613–625. DOI: http://dx.doi.org/10.3189/172756501781831864.

Hamme, RC, **Emerson, SR.** 2004. The solubility of neon, nitrogen and argon in distilled water and seawater. *Deep Sea Research Part A. Oceanographic Research Papers* **51**(11): 1517–1528. DOI: http://dx.doi.org/10.1016/j.dsr.2004.06.009.

Hansen, JW, **Thamdrup, B**, **Jørgensen, BB.** 2000. Anoxic incubation of sediment in gas-tight plastic bags: A method for biogeochemical processes studies. *Marine Ecology Progress Series* **208**: 273–282. DOI: http://dx.doi.org/10.3354/meps208273.

Johnsen, SJ, **Dahl-Jensen, D**, **Gundestrup, N**, **Steffensen, JP**, **Clausen, HB**, **Miller, H**, **Masson-Delmotte, V**, **Sveinbjörnsdottir, AE**, **White, J.** 2001. Oxygen isotope and palaeotemperature records from six Greenland ice-core stations: Camp Century, Dye-3, GRIP, GISP2, Renland and NorthGRIP. *Journal of Quaternary Science* **16**(4): 299–307. DOI: https://doi.org/10.1002/jqs.622.

Jones, SF, **Evans, GM**, **Galvin, KP.** 1999. Bubble nucleation from gas cavities—A review. *Advances in Colloid and Interface Science* **80**(1): 27–50. DOI: https://doi.org/10.1016/S0001-8686(98)00074-8.

Kawamura, T, **Jeffries, MO**, **Tison, JL**, **Krouse, HR.** 2004. Superimposed-ice formation in summer on Ross Sea pack-ice floes. *Annals of Glaciology* **39**: 563–568. DOI: http://dx.doi.org/10.3189/172756404781814168.

Kirillov, S, **Dmitrenko, I**, **Babb, D**, **Rysgaard, S**, **Barber, D.** 2015. The effect of ocean heat flux on seasonal ice growth in Young Sound (Northeast Greenland). *Journal of Geophysical Research: Oceans* **120**(7): 4803–4824. DOI: http://dx.doi.org/10.1002/2015JC010720.

Lange, MA, **Schlosser, P**, **Ackley, SF**, **Wadhams, P**, **Dieckmann, GS**. 1990. ^{18}O concentrations in sea ice of the Weddell Sea, Antarctica. *Journal of Glaciology* **36**(124): 315–323. DOI: http://dx.doi.org/10.3189/002214390793701291.

Lannuzel, D, **Tedesco, L**, **van Leeuwe, M**, **Campbell, K**, **Flores, H**, **Delille, B**, **Miller, L**, **Stefels, J**, **Assmy, P**, **Bowman, J**, **Brown, K**, **Castellani, G**, **Chierici, M**, **Crabeck, O**, **Damm, E**, **Else, B**, **Fransson, A**, **Fripiat, F**, **Geilfus, NX**, **Jacques, C**, **Jones, E**, **Kaartokallio, H**, **Kotovitch, M**, **Meiners, K**, **Moreau, S**, **Nomura, D**, **Peeken, I**, **Rintala, JM**, **Steiner, N**, **Tison, JL**, **Vancoppenolle, M**, **Van der Linden, F**, **Vichi, M**, **Wongpan, P.** 2020. The future of Arctic sea-ice biogeochemistry and ice-associated ecosystems. *Nature Climate Change* **10**(11): 983–992. DOI: http://dx.doi.org/10.1038/s41558-020-00940-4.

Lazar, B, **Loya, Y.** 1991. Bioerosion of coral reefs—A chemical approach. *Limnology and Oceanography* **36**(2): 377–383. DOI: http://dx.doi.org/10.4319/LO.1991.36.2.0377.

Leppäranta, M, **Manninen, T.** 1988. *The brine and gas content of sea ice with attention to low salinities and high temperatures*. Helsinki, Finland: Finnish Institute Marine Research Internal Report.

Loose, B, **McGillis, WR**, **Schlosser, P**, **Perovich, D**, **Takahashi, T.** 2009. Effects of freezing, growth, and ice cover on gas transport processes in laboratory seawater experiments. *Geophysical Research Letters* **36**(5): L05603. DOI: http://dx.doi.org/10.1029/2008GL036318.

Macdonald, RW, **Paton, DW**, **Carmack, EC**, **Omstedt, A.** 1995. The freshwater budget and under-ice spreading of Mackenzie River water in the Canadian Beaufort Sea based on salinity and $^{18}O/^{16}O$ measurements in water and ice. *Journal of Geophysical Research: Oceans* **100**(C1): 895–919. DOI: https://doi.org/10.1029/94JC02700.

Maksym, T, **Jeffries, MO.** 2000. A one-dimensional percolation model of flooding and snow ice formation on Antarctic sea ice. *Journal of Geophysical Research: Oceans* **105**(C11): 26313–26331. DOI: http://dx.doi.org/10.1029/2000JC900130.

Martin, S, **Kauffman, P.** 1974. The evolution of under-ice melt ponds, or double diffusion at the freezing point. *Journal of Fluid Mechanics* **64**(3): 507–528. DOI: http://dx.doi.org/10.1017/S0022112074002527.

Massom, RA, **Eicken, H**, **Haas, C**, **Jeffries, MO**, **Drinkwater, MR**, **Sturm, M**, **Worby, AP**, **Wu, XR**, **Lytle, VI**, **Ushio, S**, **Morris, K**, **Reid, PA**, **Warren, SG**, **Allison, I.** 2001. Snow on Antarctic sea ice. *Reviews of Geophysics* **39**(3): 413–445. DOI: http://dx.doi.org/10.1029/2000rg000085.

Matsuo, S, **Miyake, Y.** 1966. Gas composition in ice samples from Antarctica. *Journal of Geophysical Research: Oceans* **71**(22): 5235–5241. DOI: http://dx.doi.org/10.1029/JZ071i022p05235.

Mehrbach, C, **Culberson, CH**, **Hawley, JE**, **Pytkowicz, RM.** 1973. Measurements of the apparent dissociation constants of carbonic acid in seawater at atmospheric pressure. *Limnology and Oceanography* **18**: 897–907. DOI: http://dx.doi.org/10.4319/lo.1973.18.6.0897.

Moreau, S, **Vancoppenolle, M**, **Zhou, J**, **Tison, JL**, **Delille, B**, **Goosse, H.** 2014. Modelling argon dynamics in first-year sea ice. *Ocean Model* **73**(0): 1–18. DOI: http://dx.doi.org/10.1016/j.ocemod.2013.10.004.

National Oceanic and Atmospheric Administration. 1976. *U.S. standard atmosphere, 1976*. Washington,

DC: National Oceanic and Atmospheric Administration.

Nomura, D, **Granskog, MA**, **Assmy, P**, **Simizu, D**, **Hashida, G.** 2013. Arctic and Antarctic sea ice acts as a sink for atmospheric CO_2 during periods of snowmelt and surface flooding. *Journal of Geophysical Research: Oceans* **118**: 6511–6524. DOI: http://dx.doi.org/10.1002/2013JC009048.

Notz, D, **McPhee, MG**, **Worster, MG**, **Maykut, GA**, **Schlünzen, KH**, **Eicken, H.** 2003. Impact of underwater-ice evolution on Arctic summer sea ice. *Journal of Geophysical Research: Oceans* **108**(C7): 3223. DOI: http://dx.doi.org/10.1029/2001JC001173.

Omstedt, A. 1985. An investigation of the crystal structure of sea ice in the Bothnian Bay. RHO, Hydrologi och Oceanographi NV. Oceanography, Research Department, SMHI. Available at http://smhi.diva-portal.org/smash/get/diva2:1466824/FULLTEXT02.pdf. Accessed April 2023.

Papadimitriou, S, **Kennedy, H**, **Kattner, G**, **Dieckmann, GS**, **Thomas, DN.** 2004. Experimental evidence for carbonate precipitation and CO_2 degassing during sea ice formation. *Geochimica et Cosmochimica Acta* **68**(8): 1749–1761. DOI: http://dx.doi.org/10.1016/j.gca.2003.07.004.

Papakyriakou, TN, **Miller, LA.** 2011. Springtime CO_2 exchange over seasonal sea ice in the Canadian Arctic Archipelago. *Annals of Glaciology* **52**(57). DOI: http://dx.doi.org/10.3189/172756411795931534.

Pederson, JBT, **Kaufmann, LH**, **Kroon, A**, **Jakobsen, BH.** 2010. The Northeast Greenland sirius water polynya dynamics and variability inferred from satellite imagery. *Danish Journal of Geography* **110**(2): 131–142. DOI: http://dx.doi.org/10.1080/00167223.2010.10669503.

Perovich, DK. 1996. *The optical properties of sea ice*, Hanover, NH: Cold Regions Research & Engineering Laboratory.

Perovich, DK, **Jones, KF**, **Light, B**, **Eicken, H**, **Markus, T**, **Stroeve, J**, **Lindsay, R.** 2011. Solar partitioning in a changing Arctic sea-ice cover. *Annals of Glaciology* **52**(57): 192–196. DOI: http://dx.doi.org/10.3189/172756411795931543.

Perovich, DK, **Tucker, WB**, **Ligett, KA.** 2002. Aerial observations of the evolution of ice surface conditions during summer. *Journal of Geophysical Research: Oceans* **107**(C10): 8048. DOI: http://dx.doi.org/10.1029/2000jc000449.

Pierrot, D, **Lewis, E**, **Wallace, DWR**. 2006. MS Excel Program Developed for CO_2 System Calculations. Oak Ridge National Laboratory, Oak Ridge, Tennessee. (Carbon Dioxide Information Analysis Center). DOI: http://dx.doi.org/10.3334/CDIAC/otg.CO2SYS_XLS_CDIAC105a.

Polashenski, C, **Perovich, D**, **Courville, Z.** 2012. The mechanisms of sea ice melt pond formation and evolution. *Journal of Geophysical Research: Oceans* **117**(C1): C01001. DOI: http://dx.doi.org/10.1029/2011JC007231.

Raynaud, D, **Delmas, R**, **Ascencio, M**, **Legrand, M.** 1982. Gas extraction from polar ice cores: A critical issue for studying the evolution of atmospheric CO_2 and ice-sheet surface elevation. *Annals of Glaciology* **3**: 265–268. DOI: http://dx.doi.org/10.3189/S0260305500002895.

Rintala, JM, **Piiparinen, J**, **Blomester, J**, **Majaneva, M**, **Müller, S**, **Uusikivi, J**, **Autio, R.** 2014. Fast direct melting of brackish sea-ice samples results in biologically more accurate results than slow buffered melting. *Polar Biology* **37**(12): 1811–1822. DOI: http://dx.doi.org/10.1007/s00300-014-1563-1.

Rösel, A, **Kaleschke, L.** 2012. Exceptional melt pond occurrence in the years 2007 and 2011 on the Arctic sea ice revealed from MODIS satellite data. *Journal of Geophysical Research: Oceans* **117**. DOI: http://dx.doi.org/10.1029/2011jc007869.

Rysgaard, S, **Bendtsen, J**, **Delille, B**, **Dieckmann, GS**, **Glud, RN**, **Kennedy, H**, **Mortensen, J**, **Papadimitriou, S**, **Thomas, DN**, **Tison, JL.** 2011. Sea ice contribution to the air–sea CO_2 exchange in the Arctic and Southern Oceans. *Tellus Ser B-Chemical and Physical Meteorology* **63**(5): 823–830. DOI: http://dx.doi.org/10.1111/j.1600-0889.2011.00571.x.

Rysgaard, S, **Glud, RN.** 2004. Anaerobic N_2 production in Arctic sea ice. *Limnology and Oceanography* **49**(1): 86–94. DOI: http://dx.doi.org/10.4319/lo.2004.49.1.0086.

Rysgaard, S, **Glud, RN**, **Sejr, MK**, **Bendtsen, J**, **Christensen, PB.** 2007. Inorganic carbon transport during sea ice growth and decay: A carbon pump in polar seas. *Journal of Geophysical Research: Oceans* **112**(C03016). DOI: http://dx.doi.org/10.1029/2006JC003572.

Rysgaard, S, **Glud, RN**, **Sejr, MK**, **Blicher, ME**, **Stahl, HJ.** 2008. Denitrification activity and oxygen dynamics in Arctic sea ice. *Polar Biology* **31**: 527–537. DOI: http://dx.doi.org/10.1007/s00300-007-0384-x.

Rysgaard, S, **Søgaard, DH**, **Cooper, M**, **Pucko, M**, **Lennert, K**, **Papakyriakou, TN**, **Wang, F**, **Geilfus, NX**, **Glud, RN**, **Ehn, J**, **McGinnis, DF**, **Attard, K**, **Sievers, J**, **Deming, JW**, **Barber, D.** 2013. Ikaite crystal distribution in winter sea ice and implications for CO_2 system dynamics. *The Cryosphere* **7**(2): 707–718. DOI: http://dx.doi.org/10.5194/tc-7-707-2013.

Rysgaard, S, **Vang, T**, **Stjernholm, M**, **Rasmussen, B**, **Windelin, A**, **Kiilsholm, S.** 2003. Physical conditions, carbon transport, and climate change impacts in a northeast Greenland fjord. *Arctic, Antarctic, and Alpine Research* **35**(3): 301–312. DOI: http://dx.doi.org/10.1657/1523-0430(2003)035[0301:PCCTAC]2.0.CO;2.

Semiletov, IP, **Makshtas, A**, **Akasofu, SI**, **Andreas, EL.** 2004. Atmospheric CO_2 balance: The role of Arctic sea ice. *Geophysical Research Letters* **31**(5). DOI: http://dx.doi.org/10.1029/2003GL017996.

Søgaard, DH, **Kristensen, M**, **Rysgaard, S**, **Glud, RN**, **Hansen, PJ**, **Hilligsøe, KM.** 2010. Autotrophic and heterotrophic activity in Arctic first-year sea ice: Seasonal study from Malene Bight, SW Greenland.

Marine Ecology Progress Series **419**: 31–45. DOI: http://dx.doi.org/10.3354/meps08845.

Souchez, R, **Tison, JL**, **Jouzel, J.** 1988. Deuterium concentration and growth rate of Antarctic first-year sea ice. *Geophysical Research Letters* **15**(12): 1385–1388.

Stefels, J, **Carnat, G**, **Dacey, JWH**, **Goossens, T**, **Elzenga, JTM**, **Tison, JL.** 2012. The analysis of dimethylsulfide and dimethylsulfoniopropionate in sea ice: Dry-crushing and melting using stable isotope additions. *Marine Chemistry* **128–129**: 34–43. DOI: http://dx.doi.org/10.1016/j.marchem.2011.09.007.

Takahashi, T, **Sutherland, SC**, **Wanninkhof, R**, **Sweeney, C**, **Feely, RA**, **Chipman, DW**, **Hales, B**, **Friederich, G**, **Chavez, F**, **Sabine, C**, **Watson, A**, **Bakker, DCE**, **Schuster, U**, **Metzl, N**, **Yoshikawa-Inoue, H**, **Ishii, M**, **Midorikawa, T**, **Nojiri, Y**, **Körtzinger, A**, **Steinhoff, T**, **Hoppema, M**, **Olafsson, J**, **Arnarson, TS**, **Tilbrook, B**, **Johannessen, T**, **Olsen, A**, **Bellerby, R**, **Wong, CS**, **Delille, B**, **Bates, NR**, **de Baar, HJW.** 2009. Climatological mean and decadal change in surface ocean pCO_2, and net sea–air CO_2 flux over the global oceans. *Deep Sea Research II* **56**: 554–577. DOI: http://dx.doi.org/10.1016/j.dsr2.2008.12.009.

Taylor, PD, **Feltham, DL.** 2004. A model of melt pond evolution on sea ice. *Journal of Geophysical Research: Oceans* **109**(C12007). DOI: http://dx.doi.org/10.1029/2004jc002361.

Tison, JL, **Delille, B**, **Papadimitriou, S.** 2016. Gases in sea ice, in Thomas, DN ed., *Sea ice: Third Edition*. London, UK: John Wiley: 433–471. DOI: http://dx.doi.org/10.1002/9781118778371.ch18.

Tison, JL, **Haas, C**, **Gowing, MM**, **Sleewaegen, S**, **Bernard, A.** 2002. Tank study of physico-chemical controls on gas content and composition during growth of young sea ice. *Journal of Glaciology* **48**(161): 177–191. DOI: http://dx.doi.org/10.3189/172756502781831377.

Tison, JL, **Schwegmann, S**, **Dieckmann, G**, **Rintala, JM**, **Meyer, H**, **Moreau, S**, **Vancoppenolle, M**, **Nomura, D**, **Engberg, S**, **Blomster, LJ**, **Hendrickx, S**, **Uhlig, C**, **Luhtanen, AM**, **de Jong, J**, **Janssens, J**, **Carnat, G**, **Zhou, J**, **Delille, B.** 2017. Biogeochemical impact of snow cover and cyclonic intrusions on the winter Weddell Sea ice pack. *Journal of Geophysical Research: Oceans* **122**(12): 9548–9571. DOI: http://dx.doi.org/10.1002/2017JC013288.

Tsurikov, VL. 1979. The formation and composition of the gas content of sea ice. *Journal of Glaciology* **22**(86): 67–81. DOI: http://dx.doi.org/10.3189/S0022143000014064.

Van der Linden, FC, **Tison, JL**, **Champenois, W**, **Moreau, S**, **Carnat, G**, **Kotovitch, M**, **Fripiat, F**, **Deman, F**, **Roukaerts, A**, **Dehairs, F**, **Wauthy, S**, **Lourenço, A**, **Vivier, F**, **Haskell, T**, **Delille, B.** 2020. Sea ice CO_2 dynamics across seasons: Impact of processes at the interfaces. *Journal of Geophysical Research: Oceans* **125**(6). DOI: http://dx.doi.org/10.1029/2019JC015807.

Weeks, WF. 2010. *On sea ice*. Fairbanks, AK: Press University of Alaska.

Westwood, D. 1981. *Ammonia in waters. Methods for the examination of waters and associated materials*. London, UK: Stationery Office Books.

Woosley, RJ, **Millero, FJ**, **Takahashi, T**. 2017. Internal consistency of the inorganic carbon system in the Arctic Ocean. *Limnology and Oceanography Methods* **15**: 887–896. DOI: https://doi.org/10.1002/lom3.10208.

Yasunaka, S, **Murata, A**, **Watanabe, E**, **Chierici, M**, **Fransson, A**, **van Heuven, S**, **Hoppema, M**, **Ishii, M**, **Johannessen, T**, **Kosugi, N**, **Lauvset, SK**, **Mathis, JT**, **Nishina, S**, **Omar, AM**, **Olsen, A**, **Sasano, D**, **Takahashi, T**, **Wanninkhof, R.** 2016. Mapping of the air–sea CO_2 flux in the Arctic Ocean and its adjacent seas: Basin-wide distribution and seasonal to interannual variability. *Polar Science* **10**(3): 323–334. DOI: http://dx.doi.org/10.1016/j.polar.2016.03.006.

Zhou, J, **Delille, B**, **Brabant, F**, **Tison, JL.** 2014. Insights into oxygen transport and net community production in sea ice from oxygen, nitrogen and argon concentrations. *Biogeosciences* **11**(18): 5007–5020. DOI: http://dx.doi.org/10.5194/bg-11-5007-2014.

Zhou, J, **Delille, B**, **Eicken, H**, **Vancoppenolle, M**, **Brabant, F**, **Carnat, G**, **Geilfus, NX**, **Papakyriakou, T**, **Heinesch, B**, **Tison, JL.** 2013. Physical and biogeochemical properties in landfast sea ice (Barrow, Alaska): Insights on brine and gas dynamics across seasons. *Journal of Geophysical Research: Oceans* **118**(6): 3172–3189. DOI: http://dx.doi.org/10.1002/jgrc.20232.

How to cite this article: Geilfus, N-X, Delille, B, Tison, J-L, Lemes, M, Rysgaard, S. 2023. Gas dynamics within landfast sea ice of an Arctic fjord (NE Greenland) during the spring–summer transition. *Elementa: Science of the Anthropocene* 11(1). DOI: https://doi.org/10.1525/elementa.2022.00056

Domain Editor-in-Chief: Jody W. Deming, University of Washington, Seattle, WA, USA

Associate Editor: Christine Michel, Department of Fisheries and Oceans, University of Manitoba, Winnipeg, Canada

Knowledge Domain: Ocean Science

Part of an Elementa Special Feature: Insights into Biogeochemical Exchange Processes at Sea Ice Interfaces (BEPSII-2)

Published: April 27, 2023 **Accepted:** March 24, 2023 **Submitted:** April 19, 2022

ELEMENTA Science of the Anthropocene

Elem Sci Anth is a peer-reviewed open access journal published by University of California Press.

OPEN ACCESS